

TABLE

Comparison of device performance at each process condition for ELA and SSL

($W/L = 6 \mu m / 30 \mu m$)

	Mobility (cm^2 / Vs)	V_{th} (V)	S.S. (V /decade)
ELA	176.45	1.2	0.5
SSL	228.59	0.5	0.3



TABLE

The relationship between laser power, laser energy density and average grain size which is defined from SEM images after secco etching.

Laser power (W)	85	90	95	100	110
Laser energy density (mJ / cm ²)	392	415	438	461	507
Average grain size (μm)	0.1	0.3	0.55	0.7	1.0



TABLE

Key parameters used to simulate mobility and output characteristics with different channel geometries and laser powers.

Laser power (W)	$W (\mu m) / L (\mu m)$	$\mu_{T0} (cm^2 / Vs)$	b	m	α_{sat}
95	6 / 6	153.69	-0.16	4.8	1.38
	6 / 12	169.25	-0.22	4.3	1.24
	6 / 30	148.48	-0.12	2.5	1.13
100	6 / 6	191.84	-0.22	4.8	1.25
	6 / 12	181.32	-0.36	4.1	1.24
	6 / 30	179.44	-0.21	3.7	1.14
110	6 / 6	245.70	-0.34	4.0	1.22
	6 / 12	240.32	-0.35	6.0	1.19
	6 / 30	236.94	-0.34	3.5	1.14



TABLE

The threshold voltage (V_{th}) and on voltage (V_{on}) with their corresponding grain barrier heights at 298 K with different channel geometries and laser powers are listed.

Laser power (W)	W (μm) / L (μm)	V_{th} (V)	E_B (eV)	V_{on} (V)	E_B (eV)
95	6 / 6	0.7	0.2185	2.5	0.0706
	6 / 12	0.6	0.2072	2.0	0.0692
	6 / 30	0.6	0.2115	2.0	0.0808
100	6 / 6	0.5	0.2136	1.8	0.0722
	6 / 12	0.6	0.2115	1.9	0.0709
	6 / 30	0.5	0.2194	1.8	0.0828
110	6 / 6	0.4	0.2061	1.7	0.0735
	6 / 12	0.5	0.2293	1.6	0.0861
	6 / 30	0.5	0.2102	1.6	0.0871



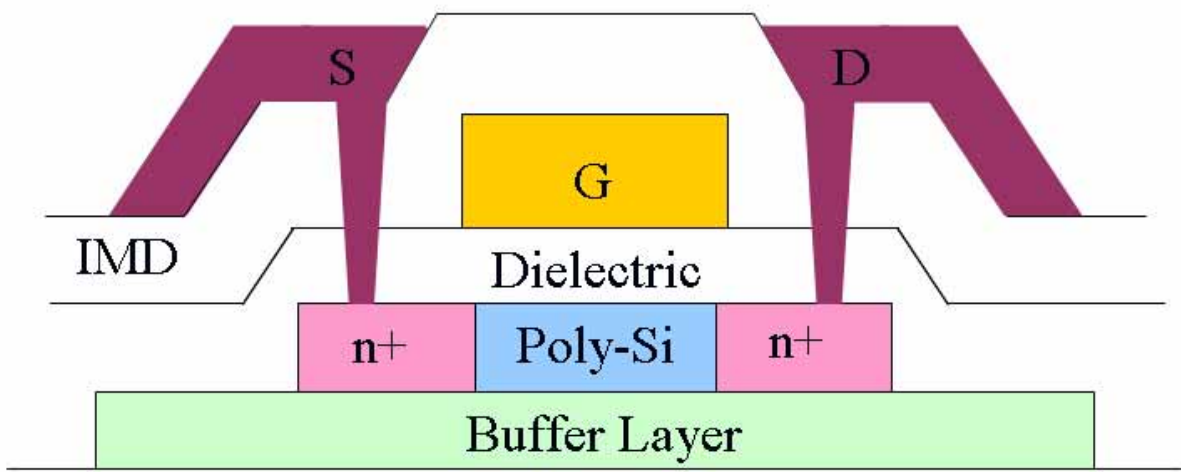


Fig. 2-1 Schematic cross sectional view of poly-Si TFT.

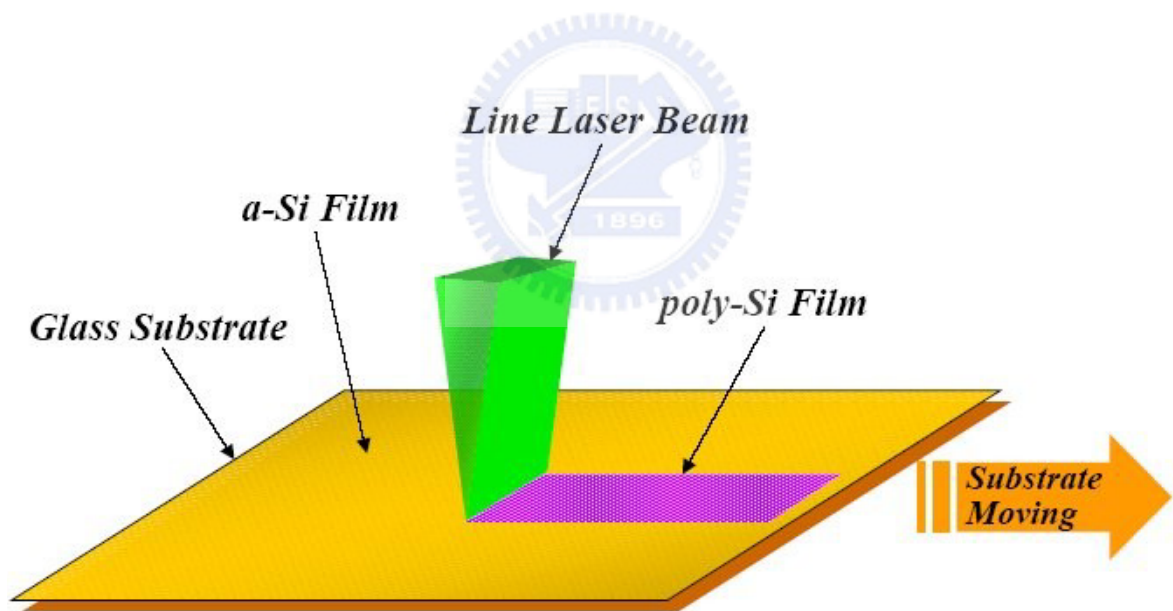


Fig. 2-2 The illustration diagram of laser annealing.

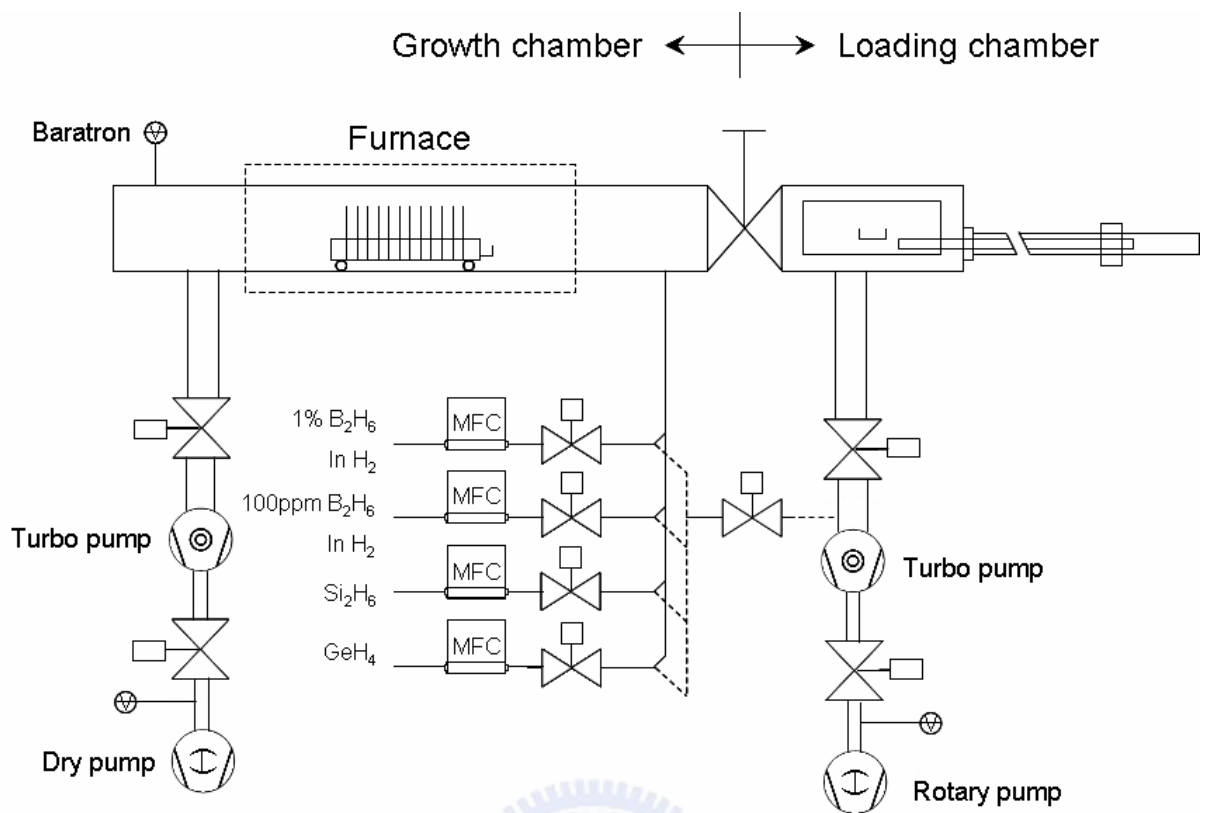


Fig. 2-3 The schematic diagram of UHVCVD system.

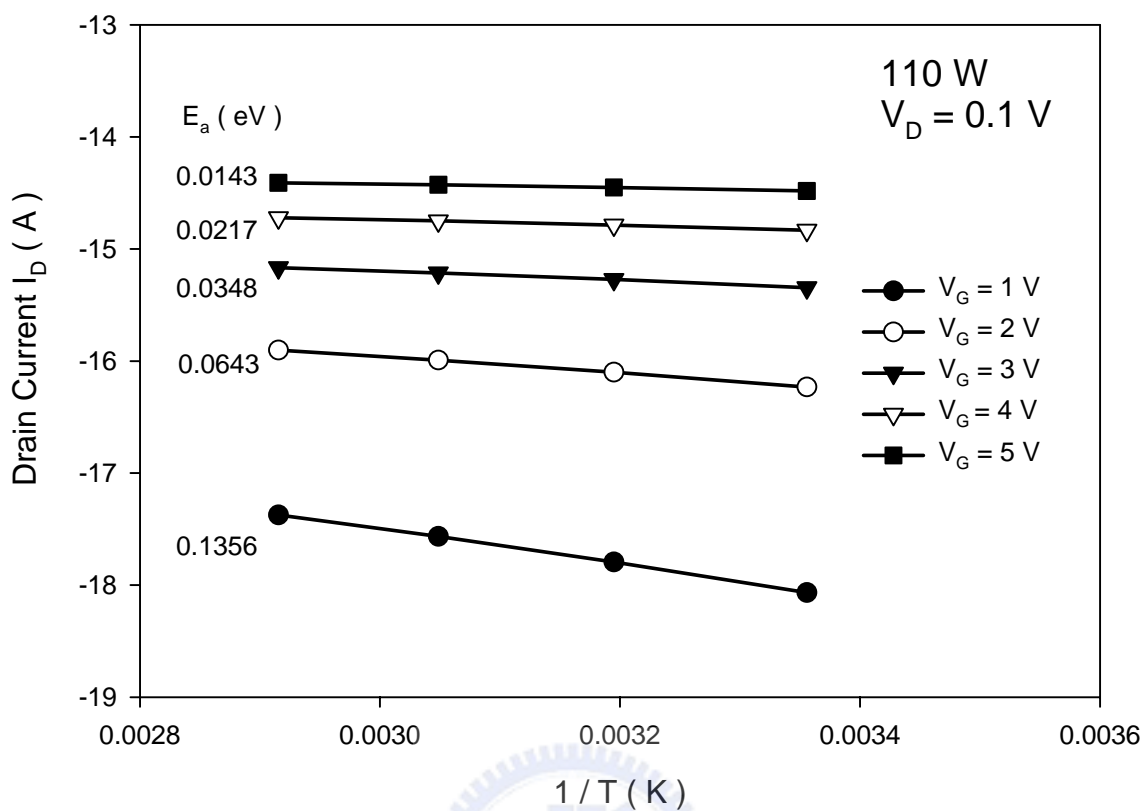


Fig. 2-4 Arrhenius Plot of the drain current of $W/L = 6 \mu m / 30 \mu m$ n-channel device for different gate voltages and $V_{DS} = 0.1 V$. The slope of each line defines the activation energy (E_a).

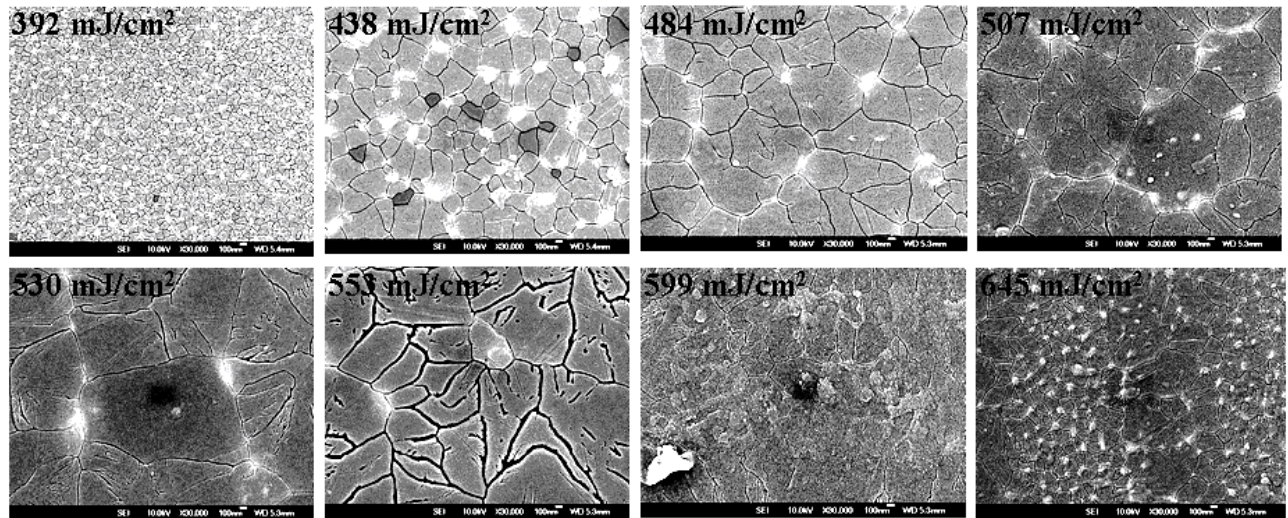


Fig. 3-1 SEM images of poly-Si grain annealed by laser energy density that varies from 392 mJ/cm^2 to 645 mJ/cm^2 .



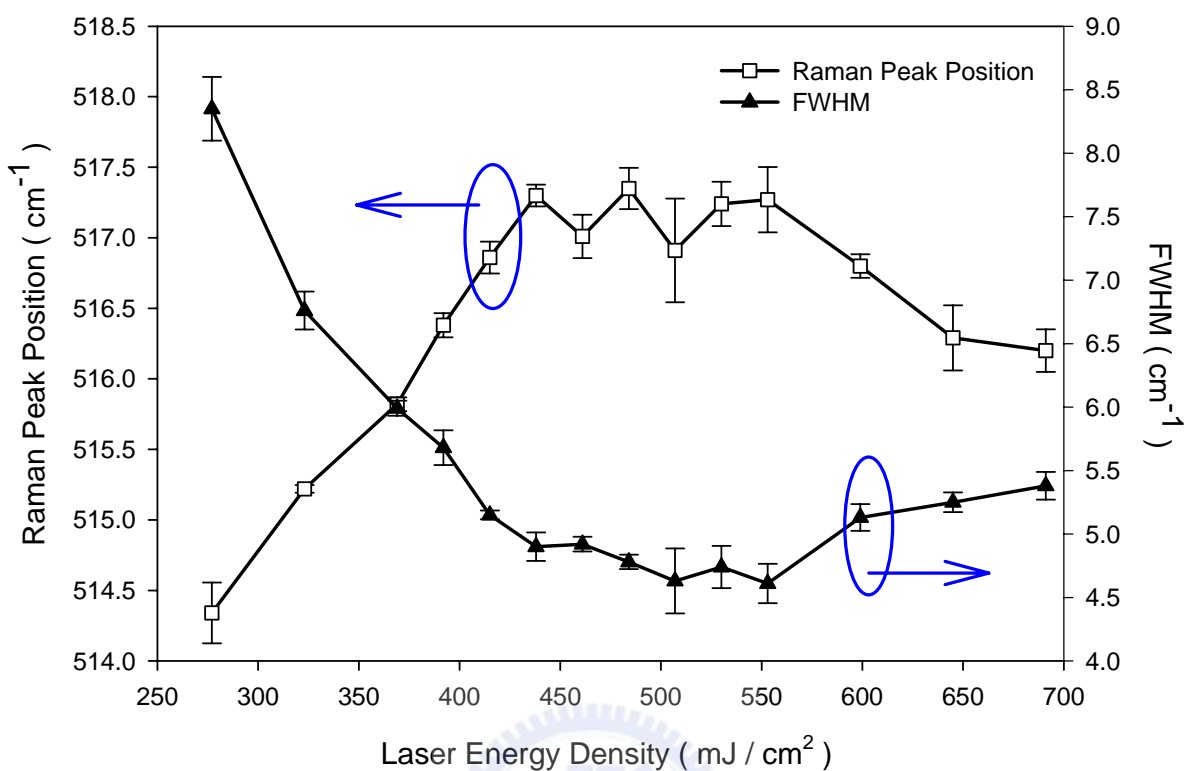


Fig. 3-2 Relationship between Raman peak position (left axis), FWHM (right axis) and laser energy density.

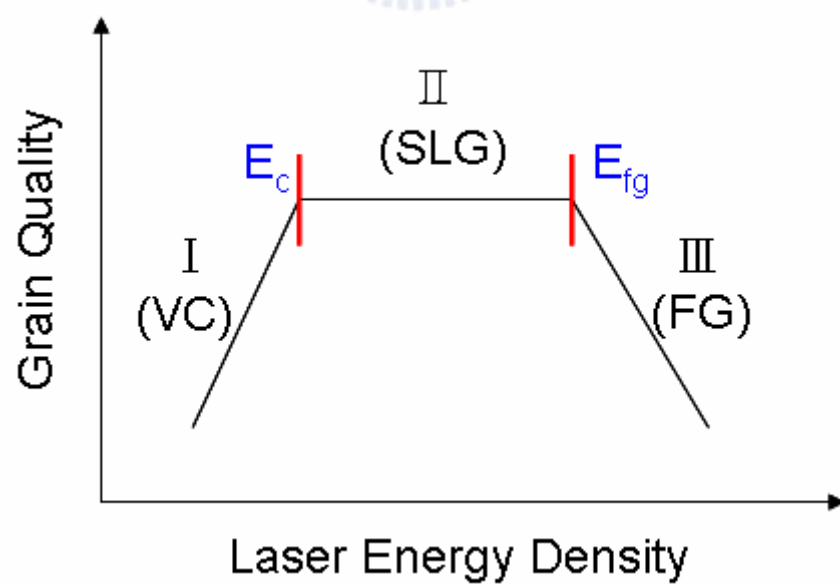


Fig. 3-3 Illustration diagram to describe the crystallization mechanism with three regions and two specific energies.

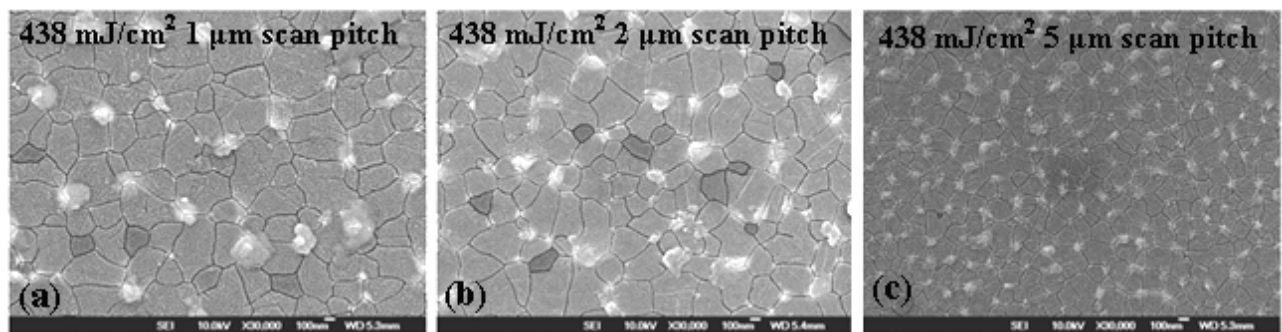


Fig. 3-4 The SEM images of poly-Si films annealed by the same laser energy density (438 mJ/cm^2) but different scan pitches ((a) $1 \mu\text{m}$, (b) $2 \mu\text{m}$ and (c) $5 \mu\text{m}$).

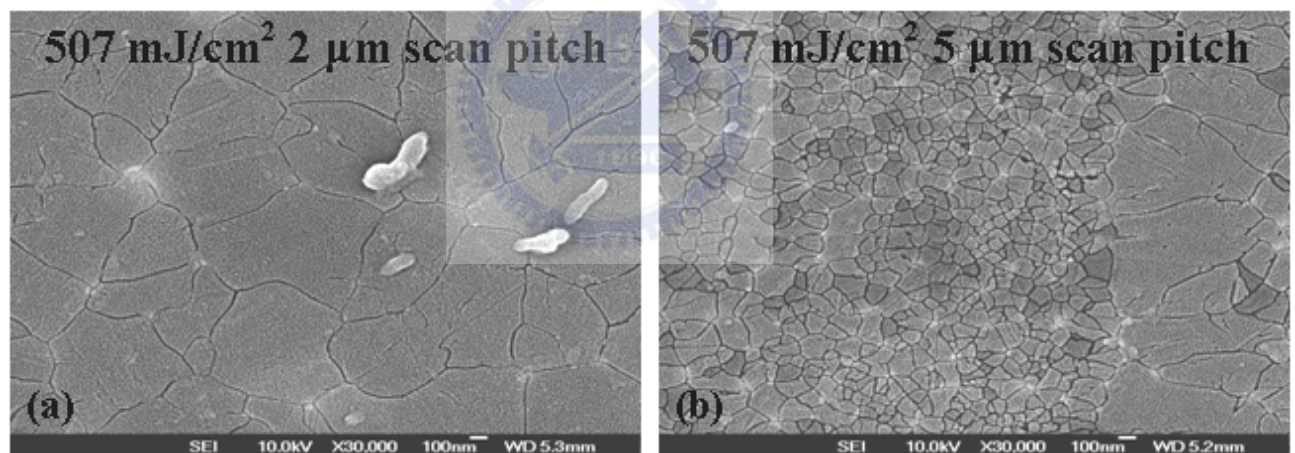


Fig. 3-5 The SEM images of poly-Si films annealed at the same laser energy density (507 mJ/cm^2) but different scan pitches ((a) $2 \mu\text{m}$ and (b) $5 \mu\text{m}$).

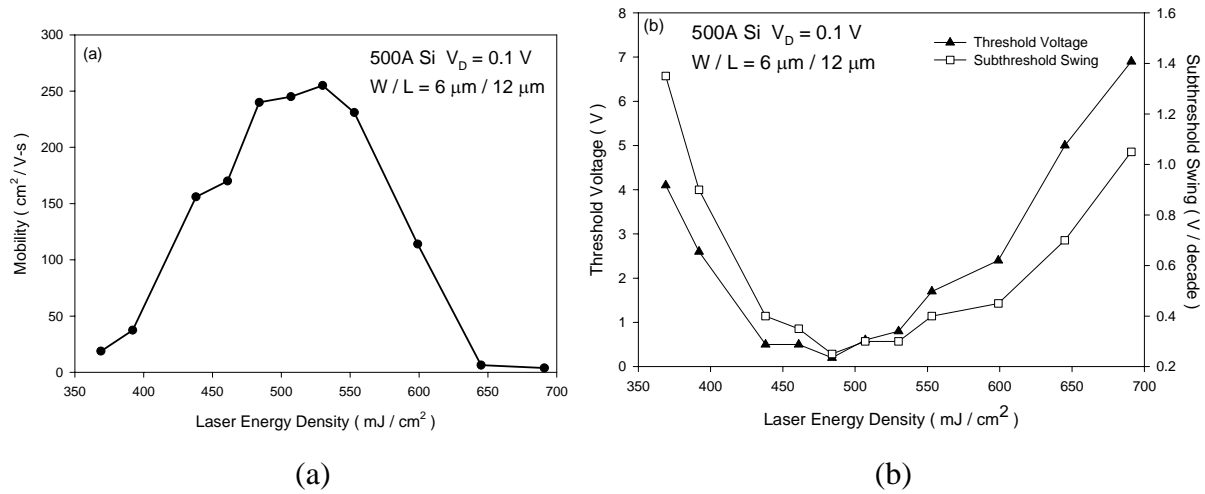


Fig. 3-6 Relationship between electrical property and laser energy density. The scan pitch is fixed to be $2 \mu\text{m}$. The active layer is 50-nm Si. The device channel width and length are $6 \mu\text{m}$ and $12 \mu\text{m}$. (a) field effect mobility (b) subthreshold swing and threshold voltage

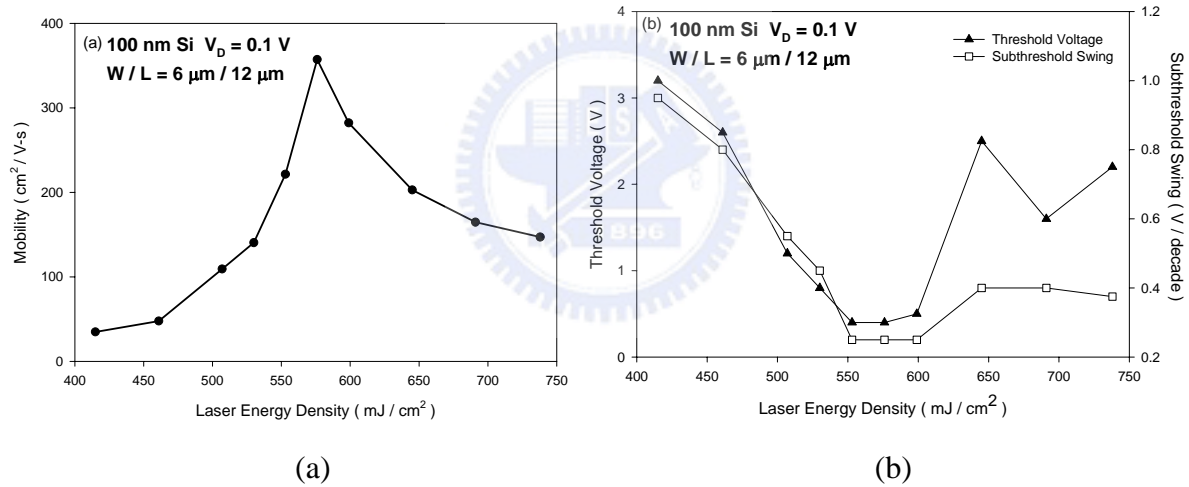


Fig. 3-7 Relationship between electrical property and laser energy density. The scan pitch is fixed to be $2 \mu\text{m}$. The active layer is 100-nm Si. The device channel width and length are $6 \mu\text{m}$ and $12 \mu\text{m}$. (a) field effect mobility (b) subthreshold swing and threshold voltage

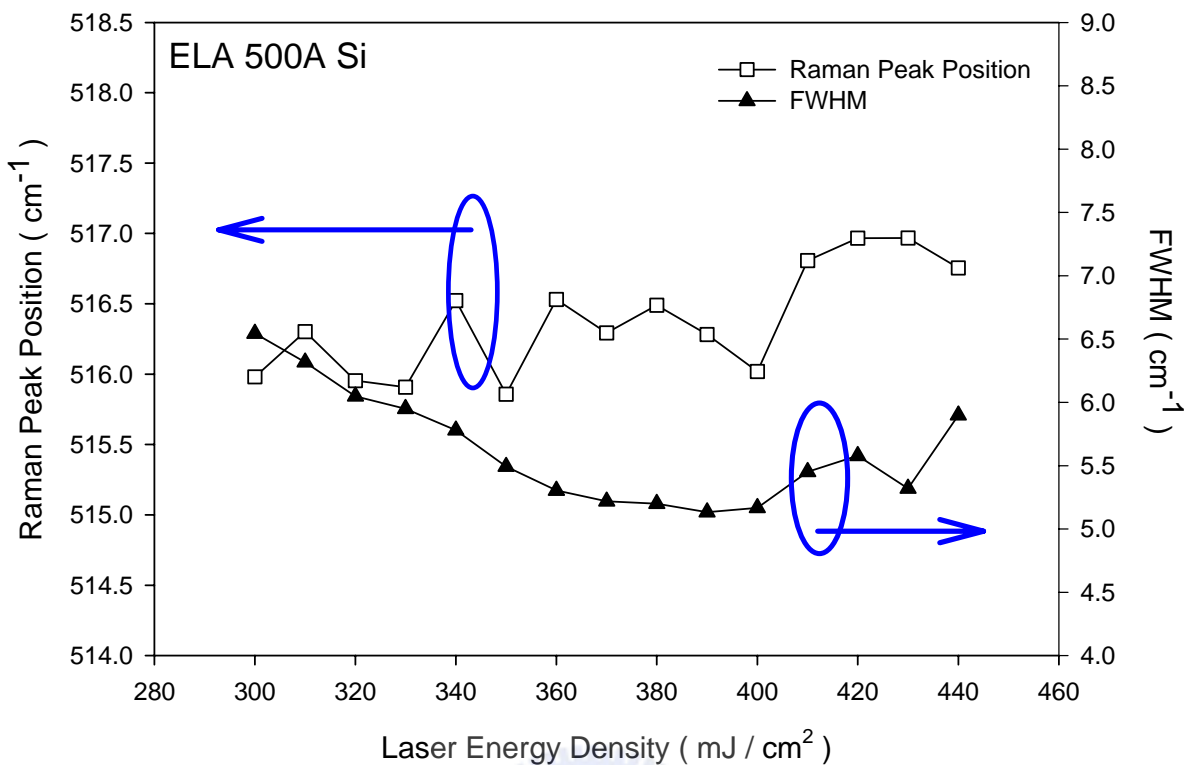
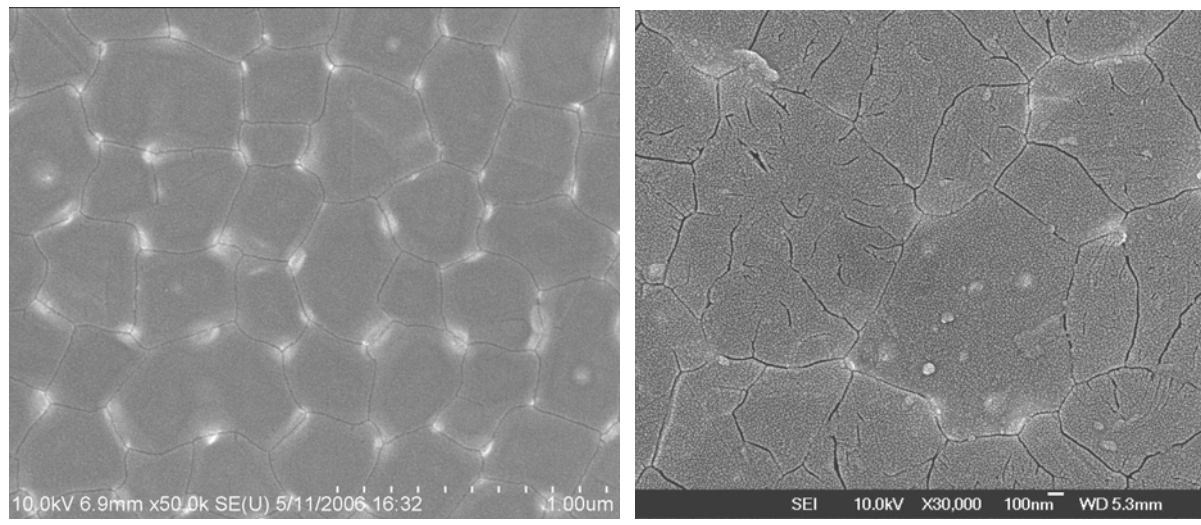


Fig. 3-8 The Raman peak positions and FWHM versus laser energy density of 50-nm Si annealed by ELA.



(a)

(b)

Fig. 3-9 The SEM images after secco etching of 50-nm Si annealed by ELA and SSL at each process laser energy density. (a) ELA (b) SSL

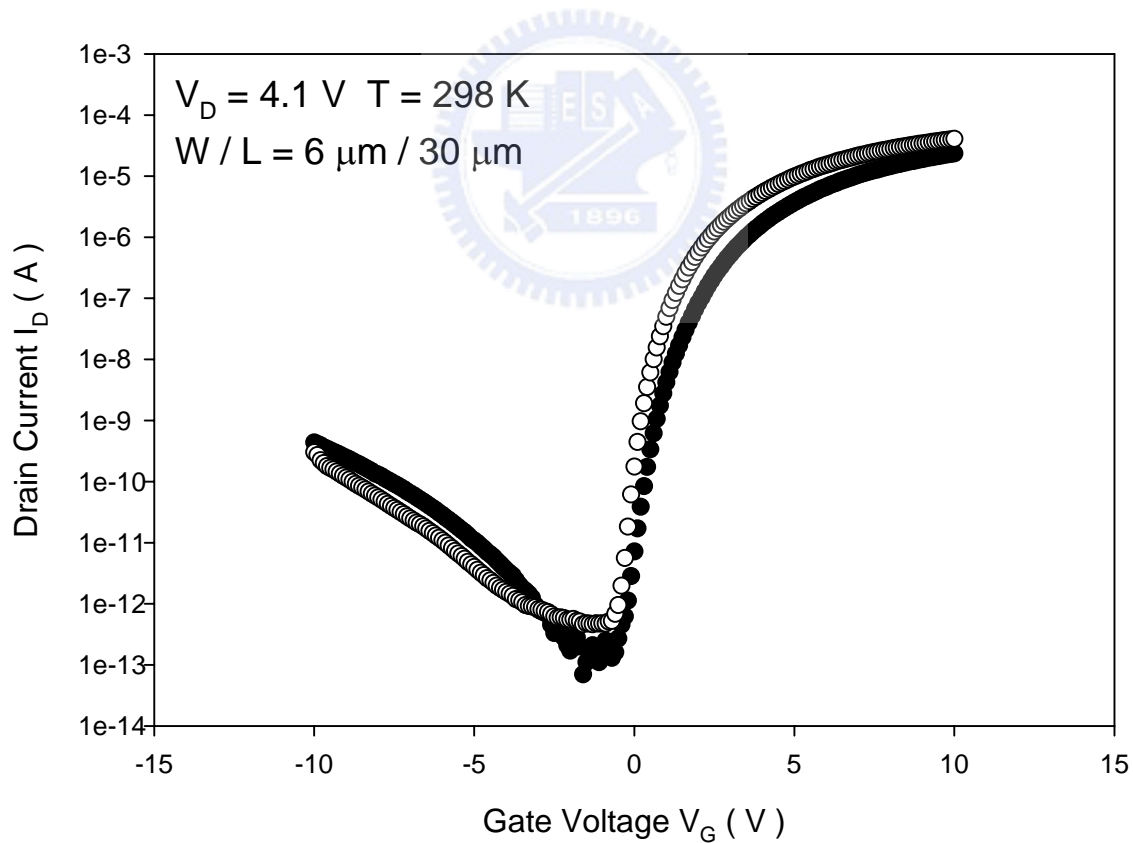


Fig. 3-10 Comparison of typical transfer characteristic for n-channel poly-Si TFTs annealed by ELA and SSL at each best laser condition.

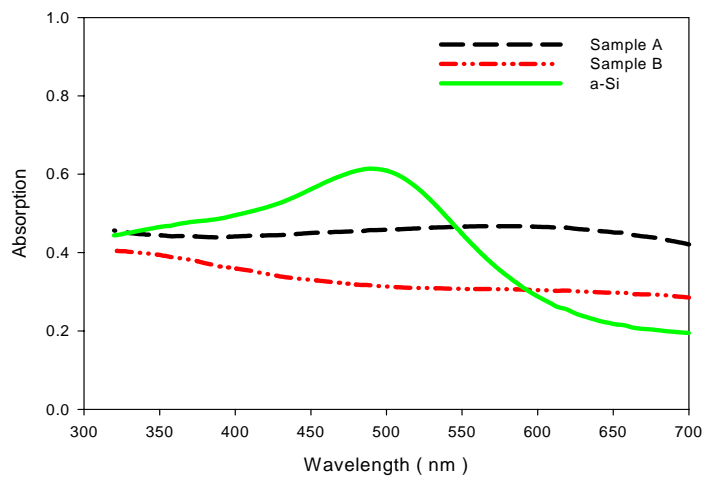


Fig. 3-11 The light absorption versus wavelength of a-Si and a-SiGe thin film.

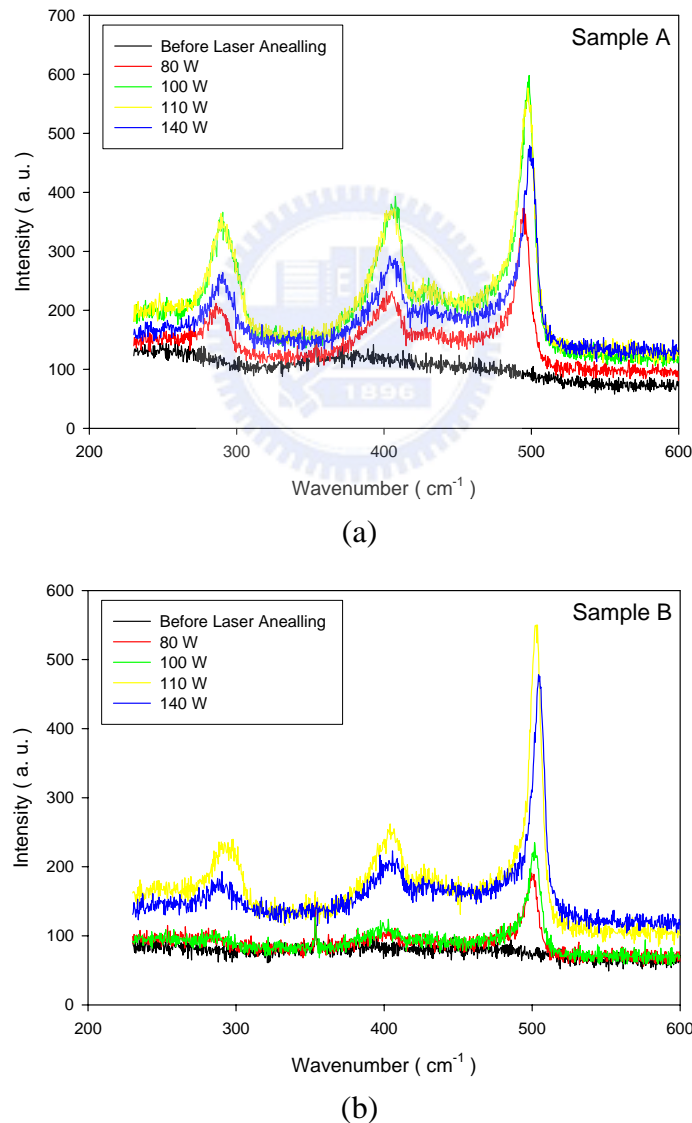


Fig. 3-12 Raman spectra obtained on a-SiGe thin films before and after laser irradiations performed in different conditions. (a) sample A (b) sample B

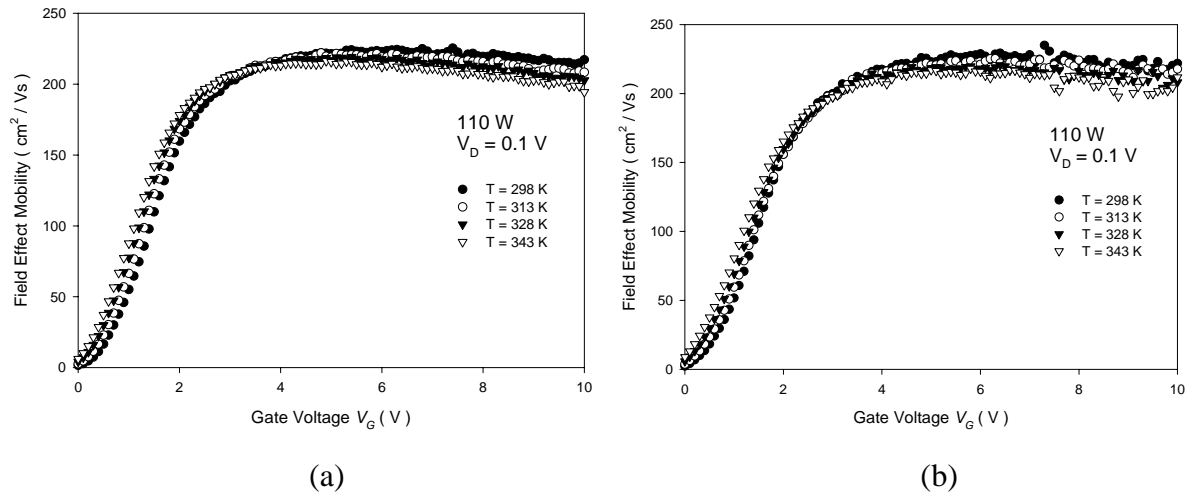


Fig. 3-13 The field effect mobility versus gate voltage at different temperature for n-channel TFT with various geometries. (a) $W/L = 6 \mu\text{m} / 30 \mu\text{m}$ (b) $W/L = 6 \mu\text{m} / 6 \mu\text{m}$

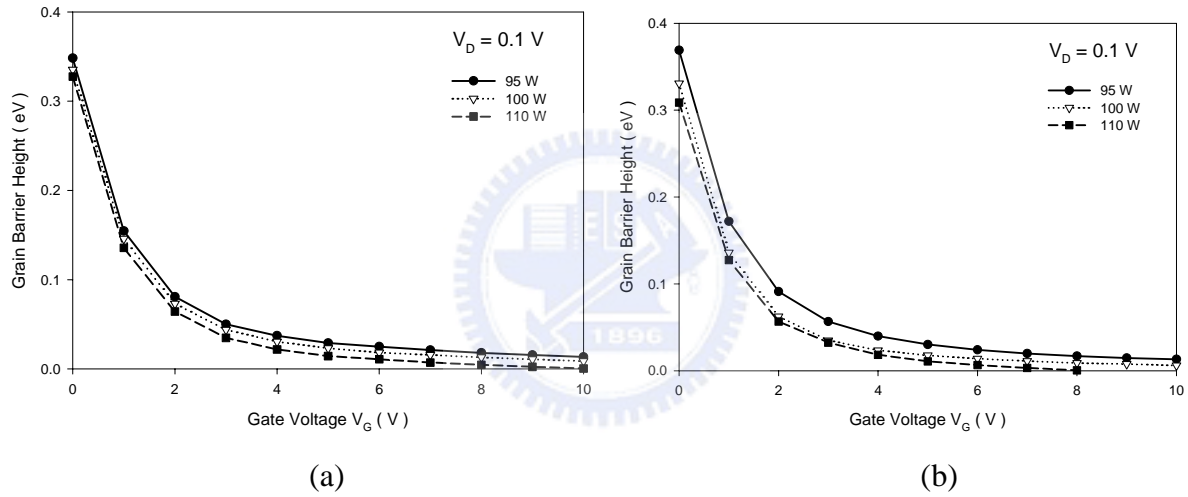


Fig. 3-14 The relationship of grain barrier height versus gate voltage for different laser energies. (a) $W/L = 6 \mu\text{m} / 30 \mu\text{m}$ (b) $W/L = 6 \mu\text{m} / 6 \mu\text{m}$

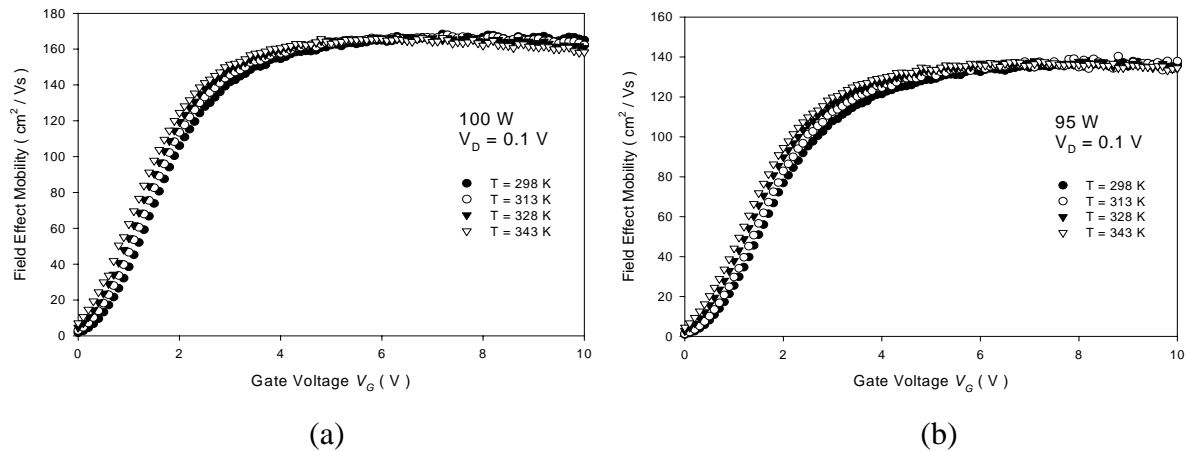
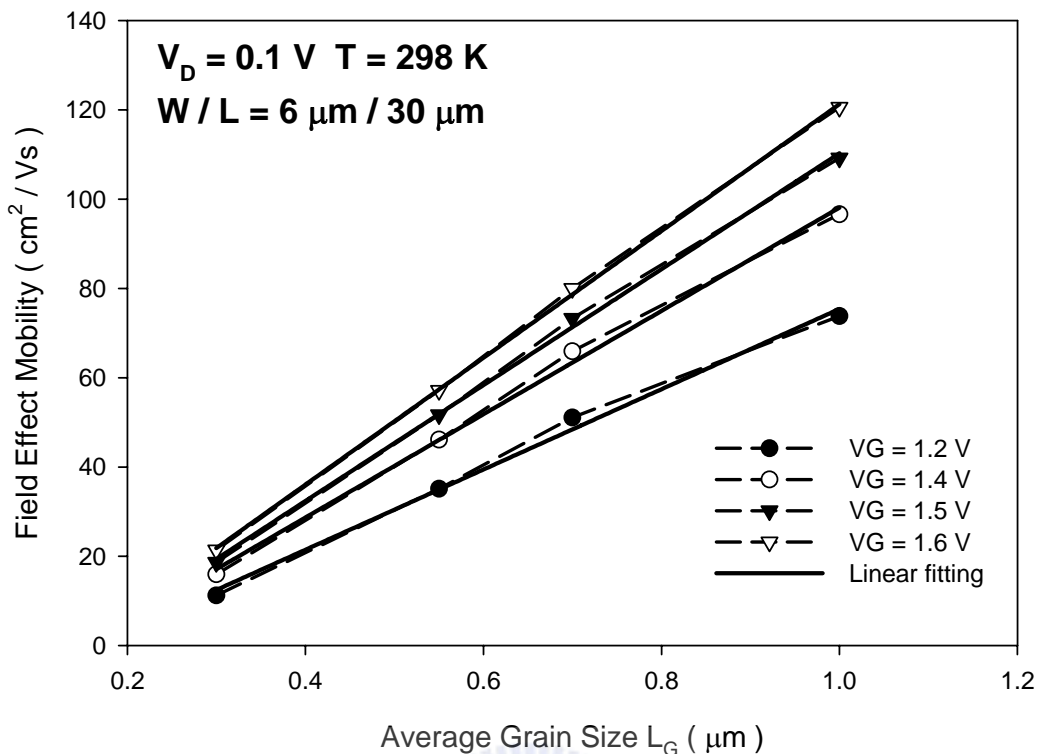
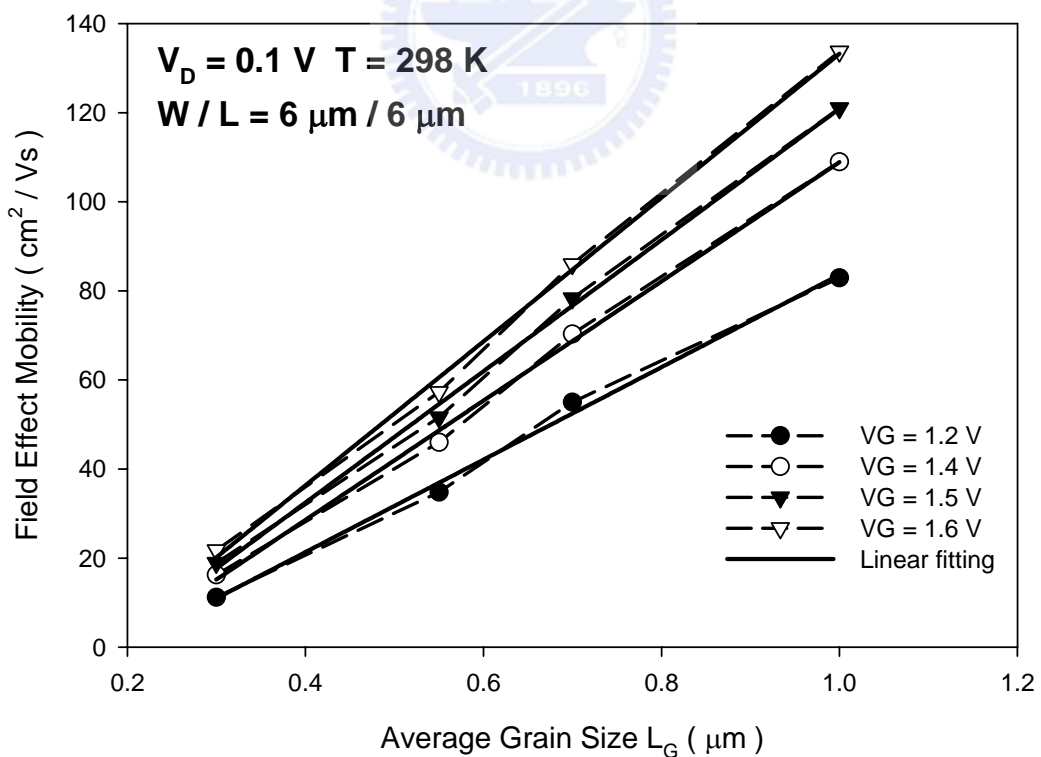


Fig. 3-15 The field effect mobility versus gate voltage at different temperature for two laser energies. ($W/L = 6 \mu\text{m} / 30 \mu\text{m}$) (a) 100 W (b) 95 W



(a)



(b)

Fig. 3-16 The mobility versus average grain size at various low gate voltage biases for different channel lengths. (a) $W/L = 6 \mu\text{m} / 30 \mu\text{m}$ (b) $W/L = 6 \mu\text{m} / 6 \mu\text{m}$

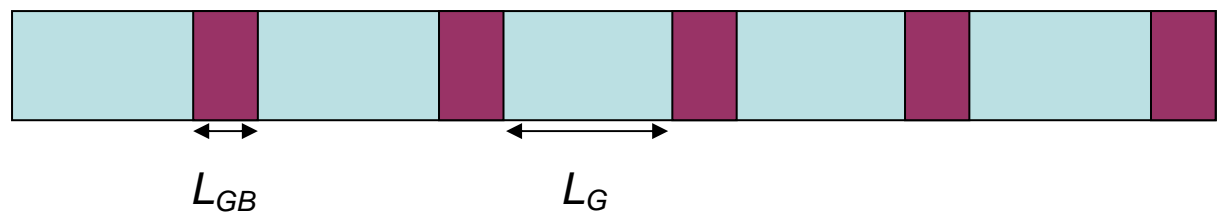


Fig. 3-17 The illustration diagram of grain and grain boundary for mobility modeling.



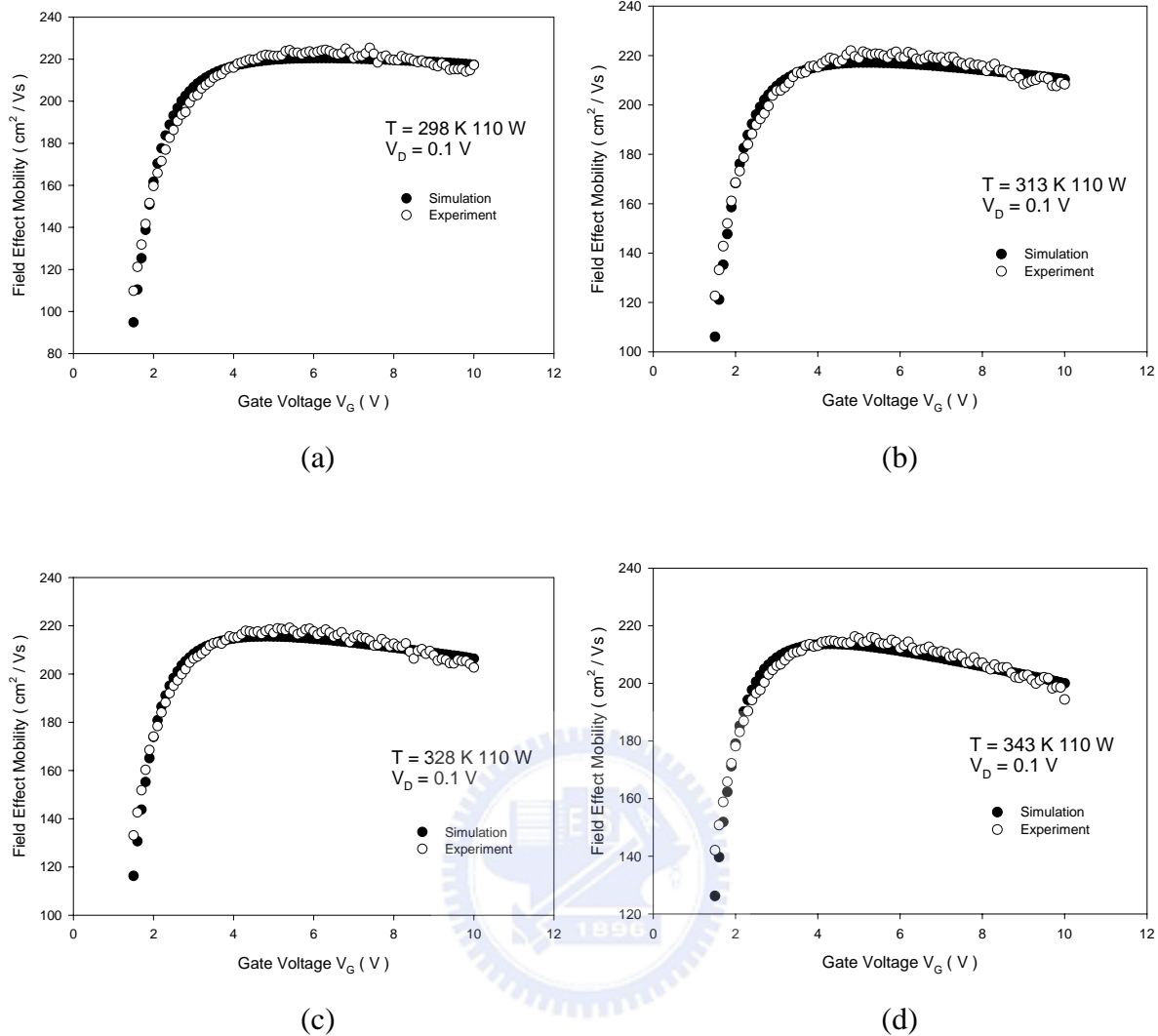


Fig. 3-18 Comparison of field effect mobility between the simulation results and experiment data at different temperatures. ($W/L = 6\text{ }\mu\text{m} / 30\text{ }\mu\text{m}$) (a) $T = 298\text{ K}$ (b) $T = 313\text{ K}$ (c) $T = 328\text{ K}$ (d) $T = 343\text{ K}$

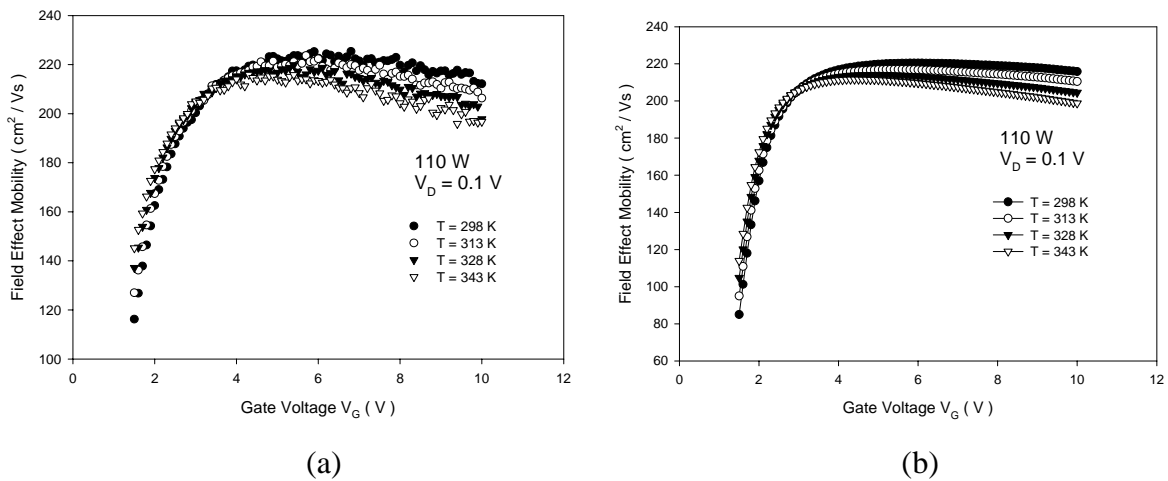


Fig. 3-19 The field effect mobility versus gate voltage at different temperatures. ($W/L = 6 \mu\text{m} / 12 \mu\text{m}$) (a) experiment (b) simulation

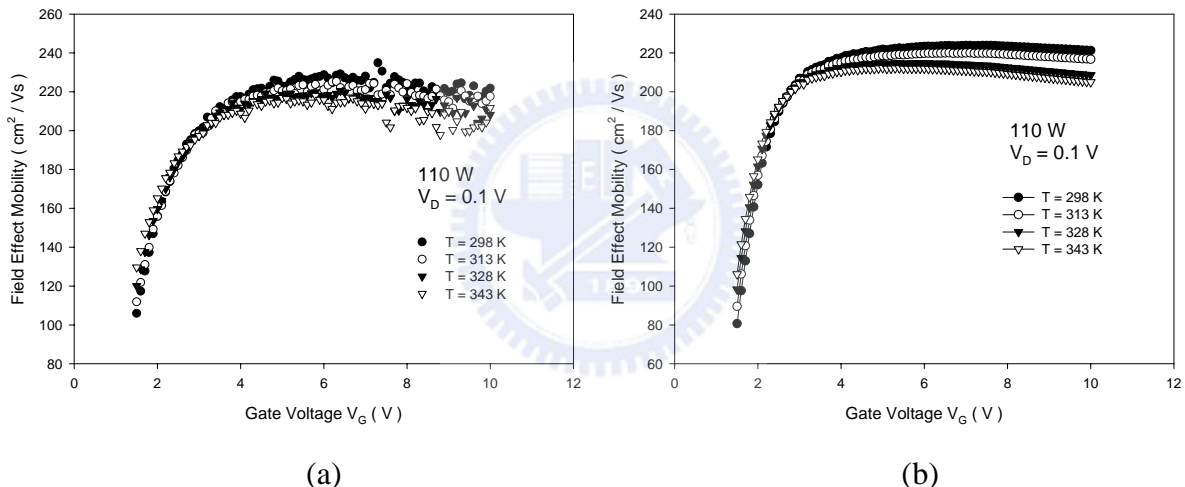


Fig. 3-20 The field effect mobility versus gate voltage at different temperatures. ($W/L = 6 \mu\text{m} / 6 \mu\text{m}$) (a) experiment (b) simulation

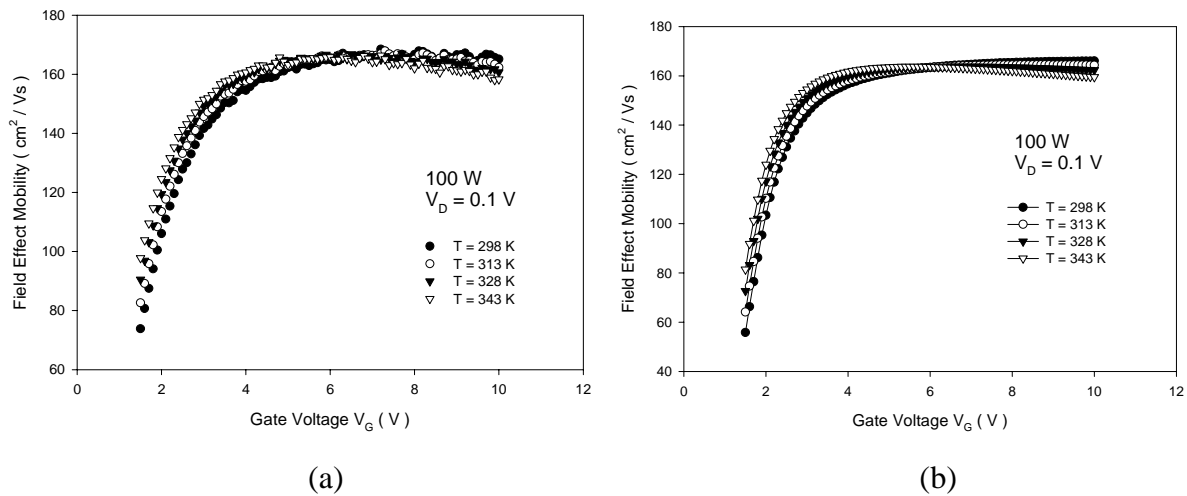


Fig. 3-21 The field effect mobility versus gate voltage at different temperatures. ($W/L = 6 \mu\text{m} / 30 \mu\text{m}$) (a) experiment (b) simulation

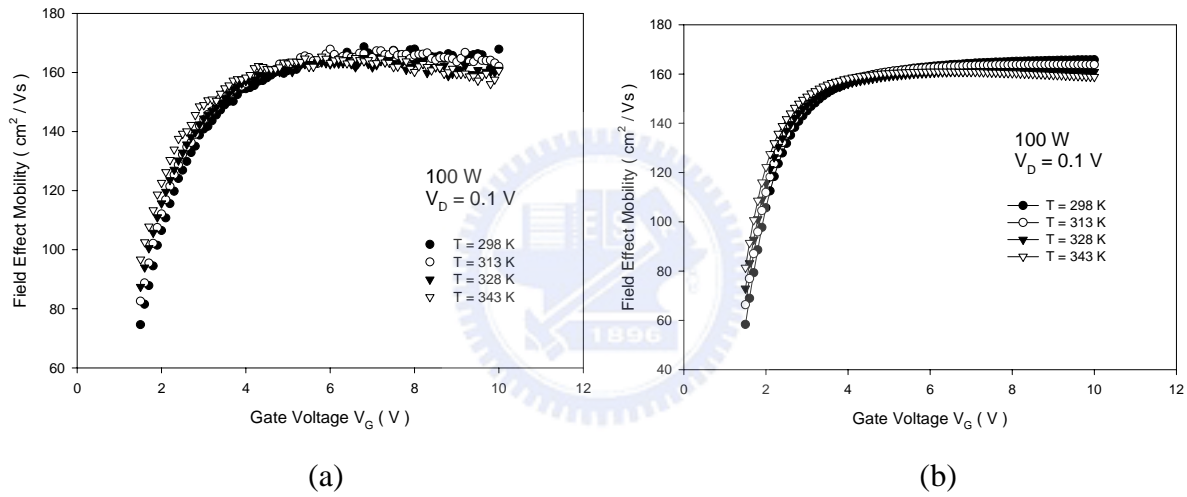


Fig. 3-22 The field effect mobility versus gate voltage at different temperatures. ($W/L = 6 \mu\text{m} / 12 \mu\text{m}$) (a) experiment (b) simulation

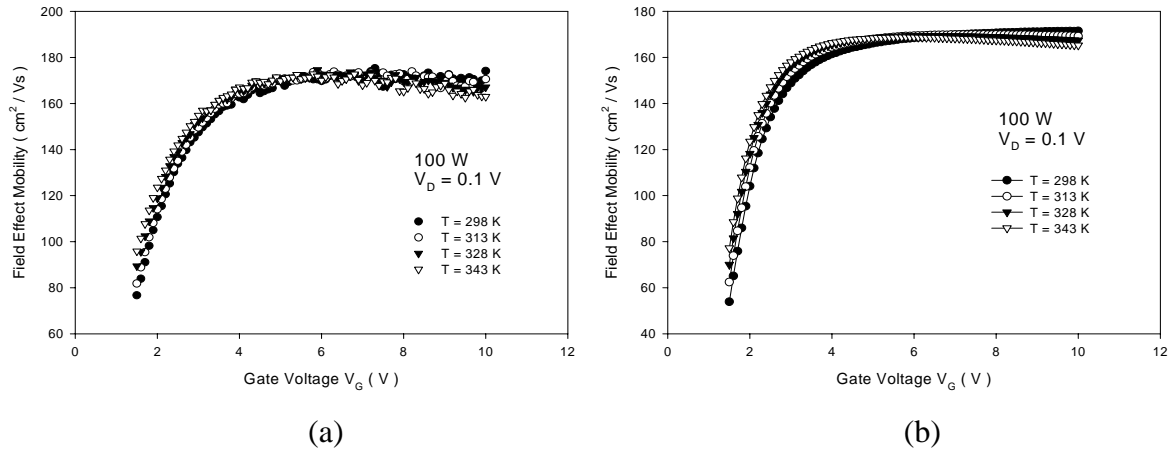


Fig. 3-23 The field effect mobility versus gate voltage at different temperatures. ($W/L = 6 \mu\text{m} / 6 \mu\text{m}$) (a) experiment (b) simulation

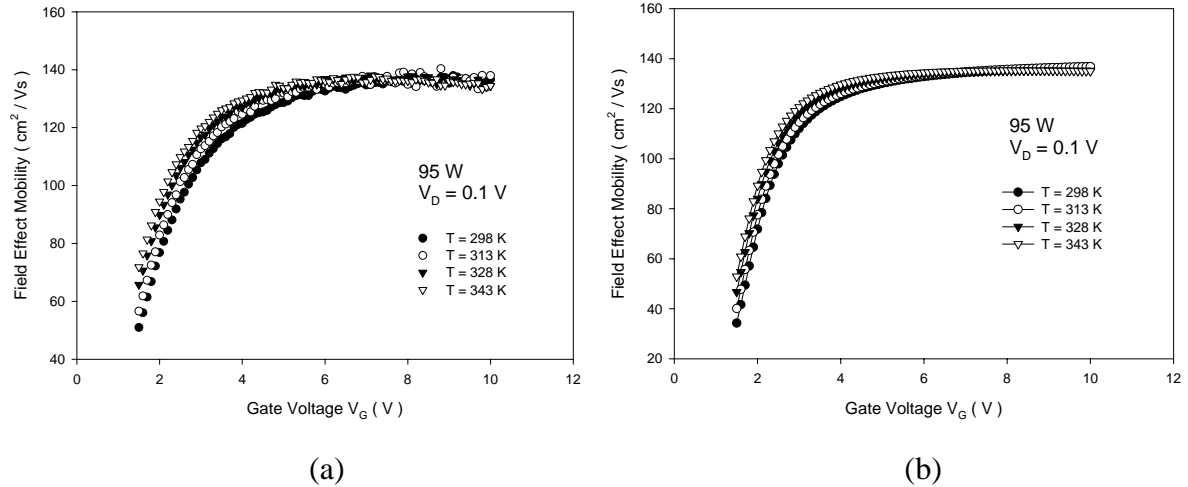


Fig. 3-24 The field effect mobility versus gate voltage at different temperatures. ($W/L = 6 \mu\text{m} / 30 \mu\text{m}$) (a) experiment (b) simulation

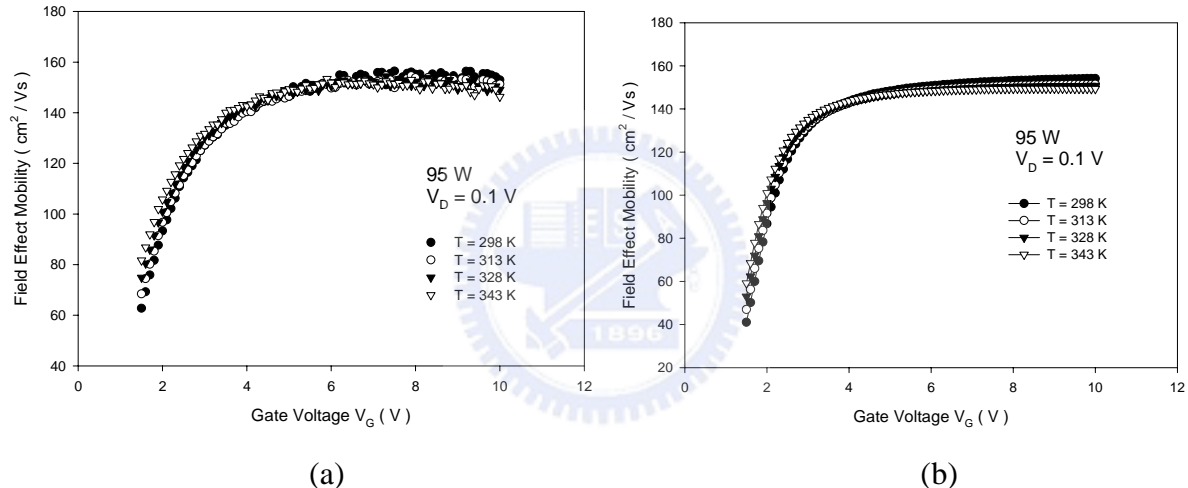


Fig. 3-25 The field effect mobility versus gate voltage at different temperatures. ($W/L = 6 \mu\text{m} / 12 \mu\text{m}$) (a) experiment (b) simulation

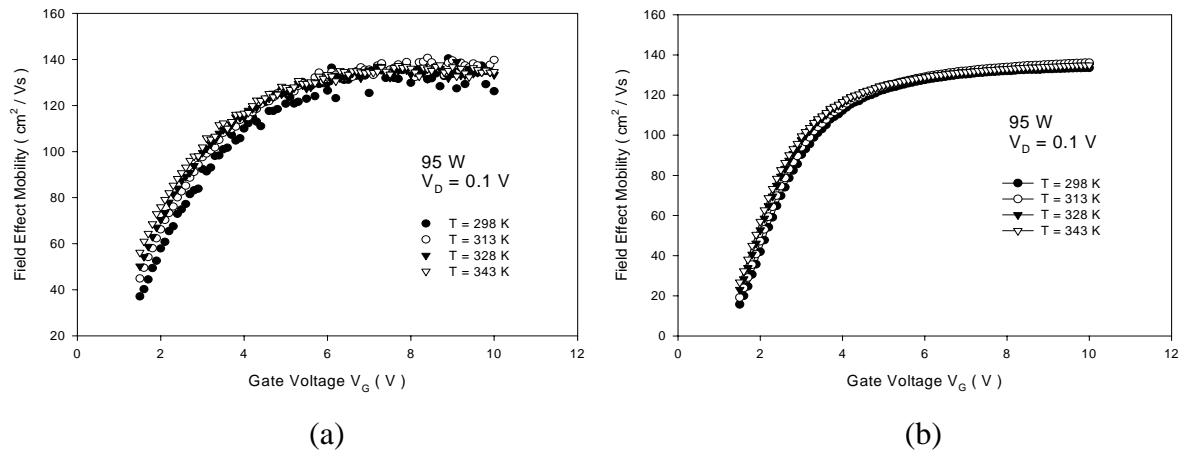
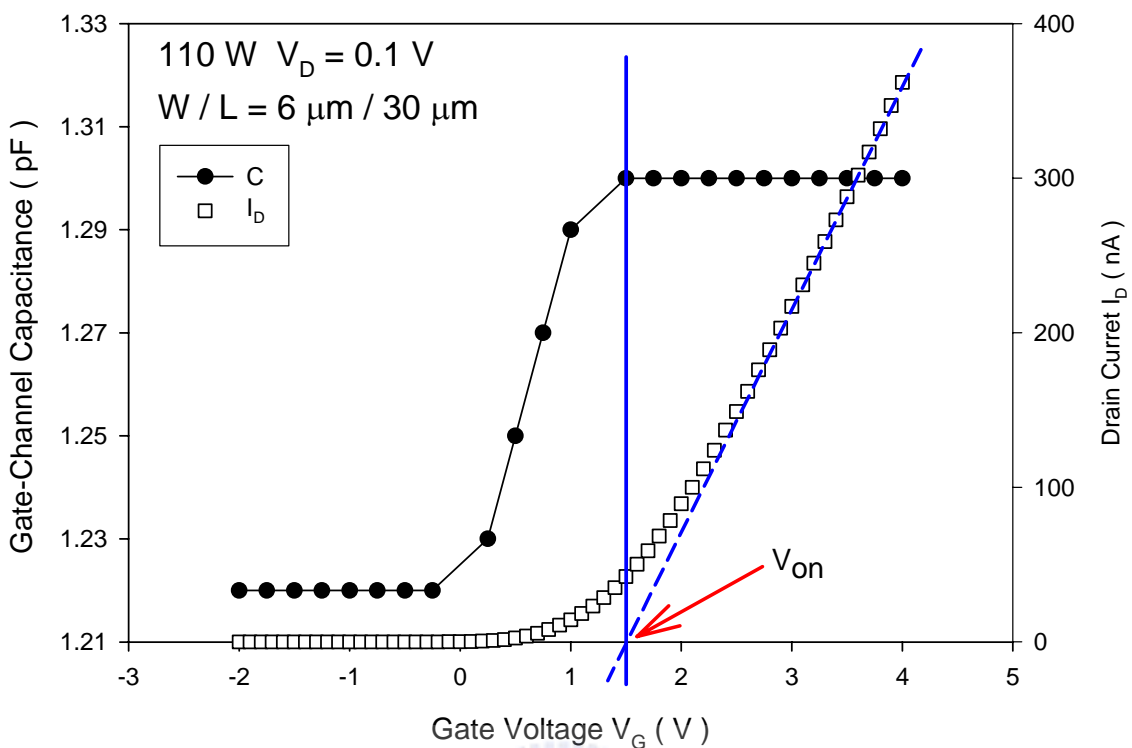
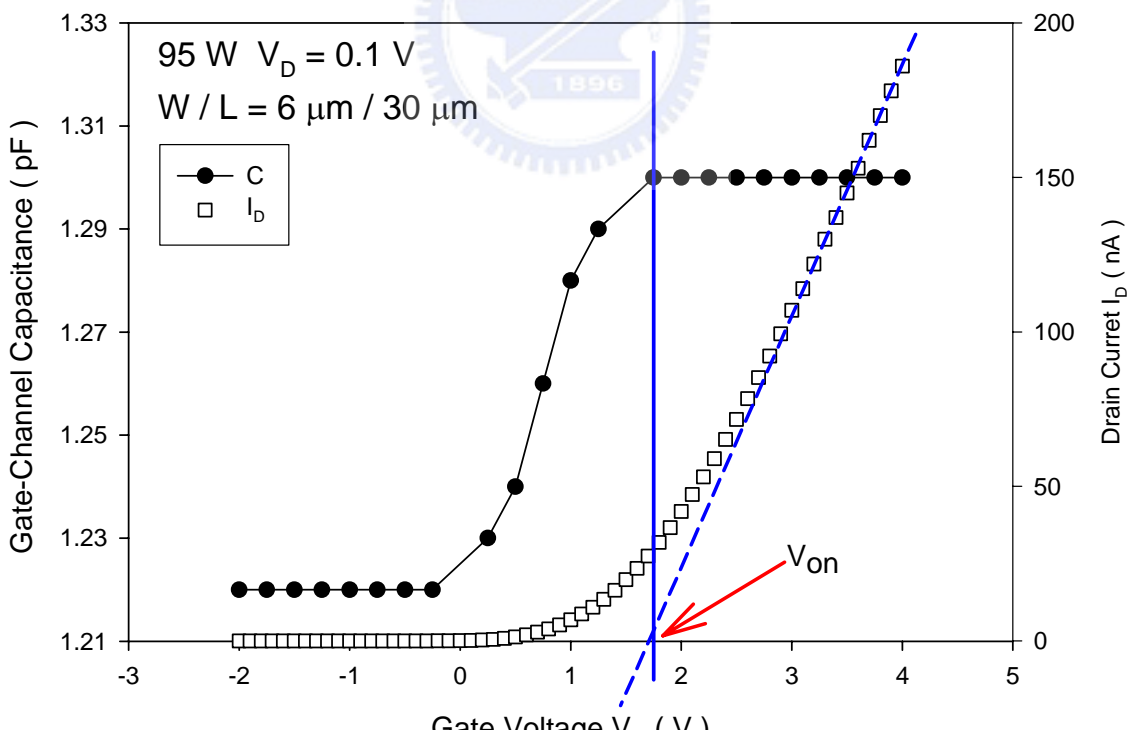


Fig. 3-26 The field effect mobility versus gate voltage at different temperatures. ($W/L = 6 \mu\text{m} / 6 \mu\text{m}$) (a) experiment (b) simulation



(a)



(b)

Fig. 3-27 The $C-V$ and transfer characteristics of devices annealed by different laser energies are put together to determine V_{on} . ($W/L = 6 \mu\text{m} / 30 \mu\text{m}$) (a) 110 W (b) 95 W

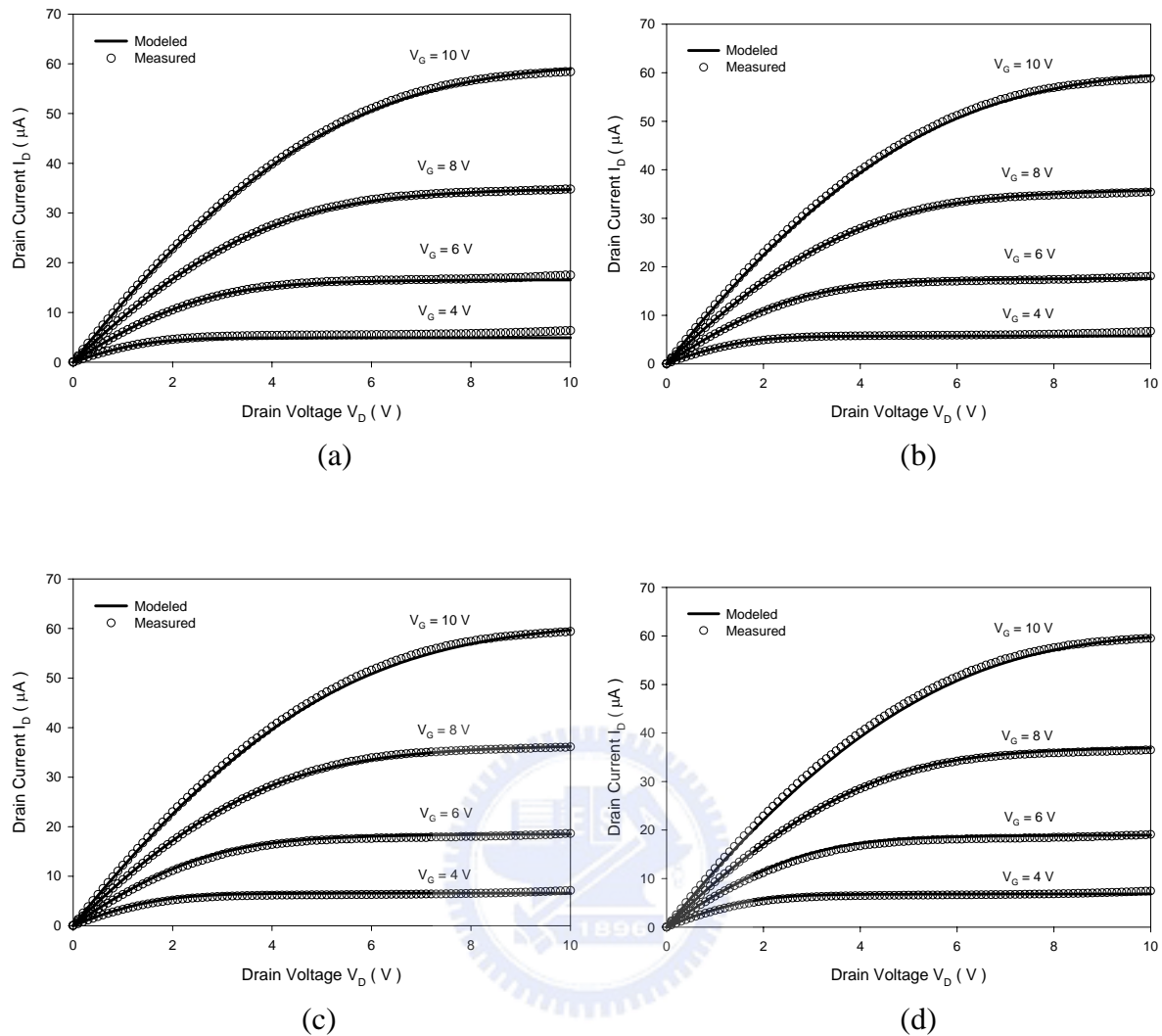


Fig. 3-28 The comparison of measured (symbols) and modeled (solid line) I - V output characteristics for $W/L = 6 \mu\text{m} / 30 \mu\text{m}$ n-channel poly-Si TFTs annealed with laser power 110 W. (a) $T = 298 \text{ K}$ (b) $T = 313 \text{ K}$ (c) $T = 328 \text{ K}$ (d) $T = 343 \text{ K}$

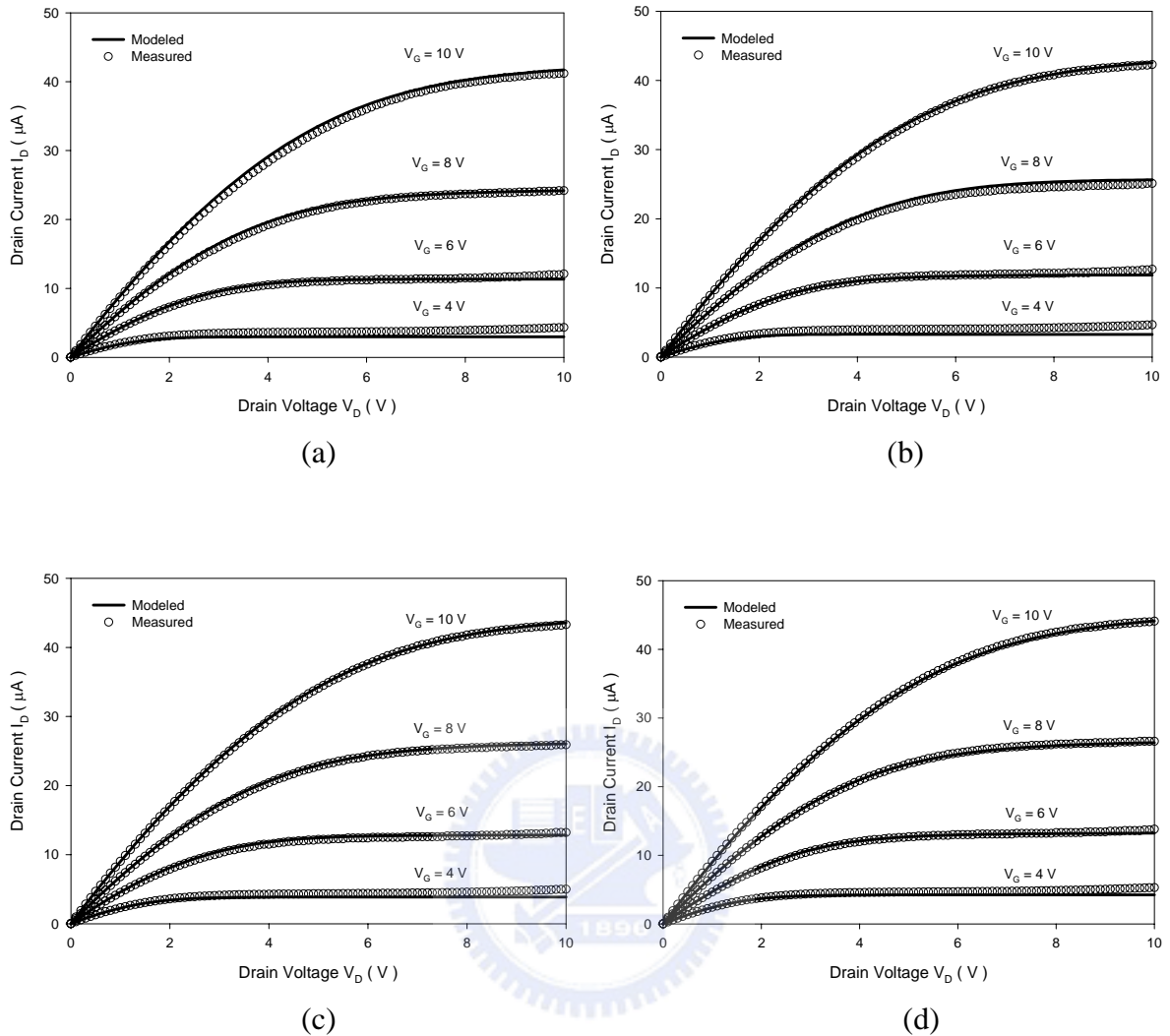


Fig. 3-29 The comparison of measured (symbols) and modeled (solid line) I - V output characteristics for $W/L = 6 \mu\text{m} / 30 \mu\text{m}$ n-channel poly-Si TFTs annealed with laser power 100 W. (a) $T = 298 \text{ K}$ (b) $T = 313 \text{ K}$ (c) $T = 328 \text{ K}$ (d) $T = 343 \text{ K}$

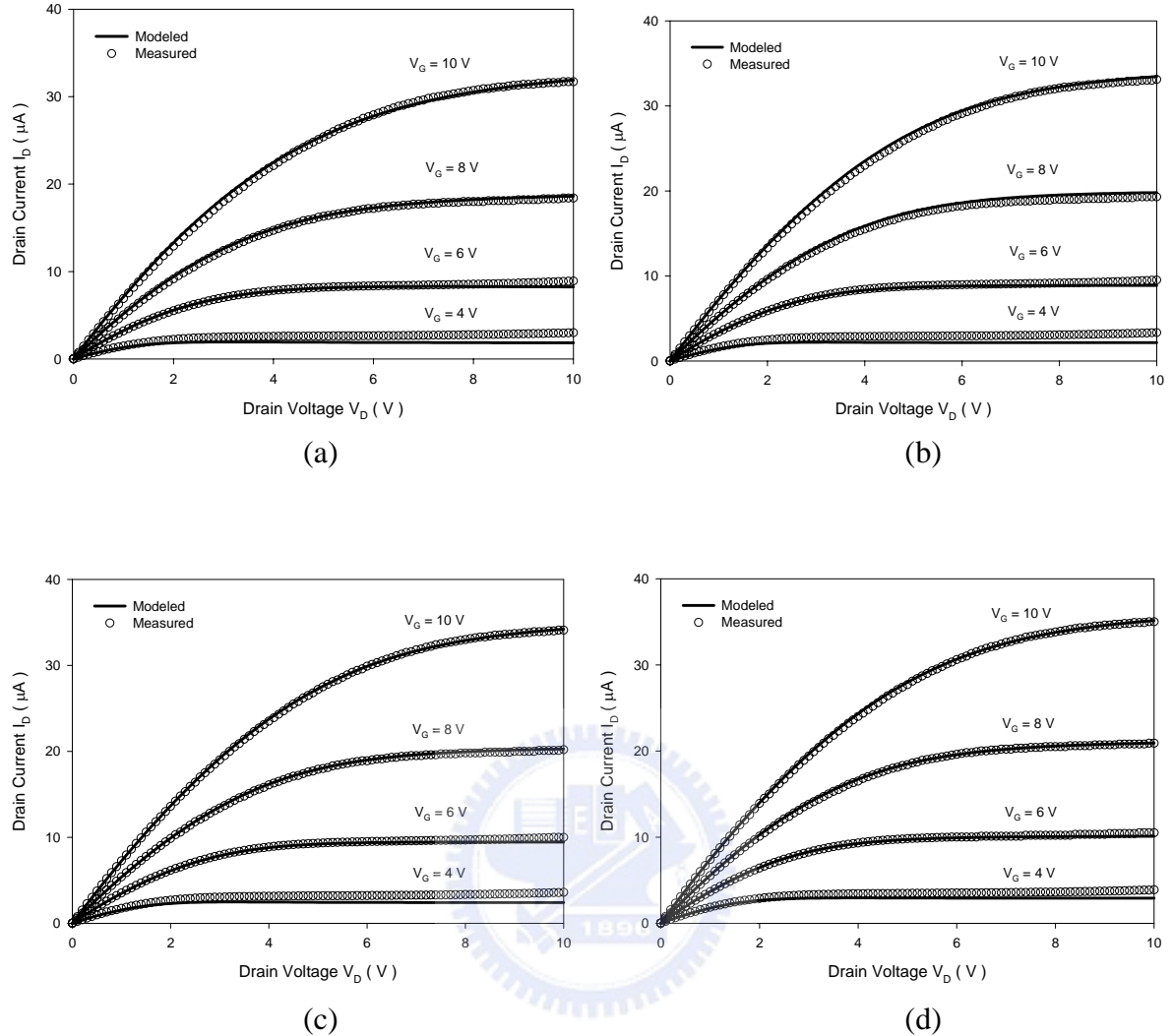


Fig. 3-30 The comparison of measured (symbols) and modeled (solid line) $I-V$ output characteristics for $W/L = 6 \mu\text{m} / 30 \mu\text{m}$ n-channel poly-Si TFTs annealed with laser power 95 W. (a) $T = 298 \text{ K}$ (b) $T = 313 \text{ K}$ (c) $T = 328 \text{ K}$ (d) $T = 343 \text{ K}$

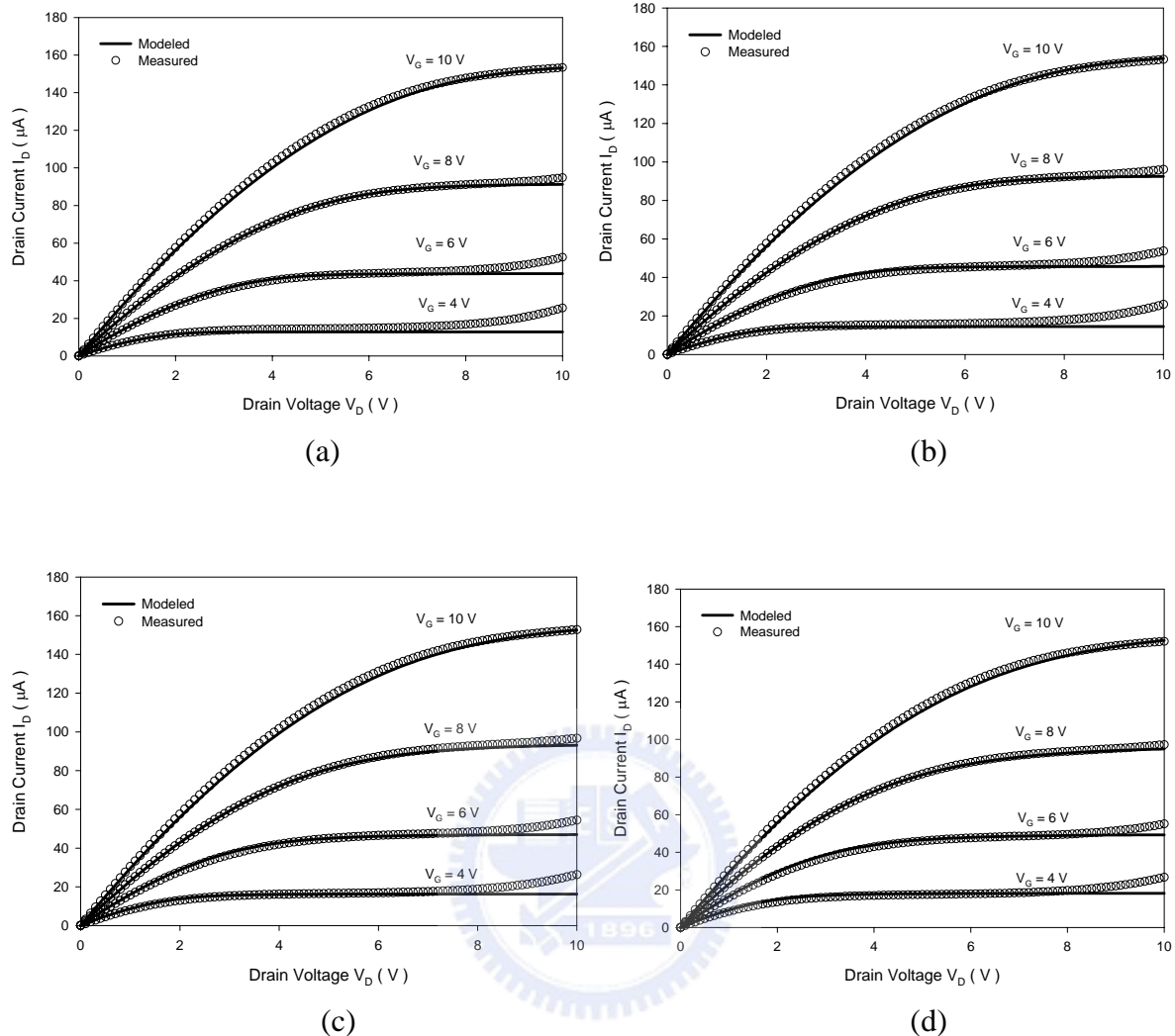


Fig. 3-31 The comparison of measured (symbols) and modeled (solid line) $I-V$ output characteristics for $W/L = 6 \mu\text{m} / 12 \mu\text{m}$ n-channel poly-Si TFTs annealed with laser power 110 W . (a) $T = 298 \text{ K}$ (b) $T = 313 \text{ K}$ (c) $T = 328 \text{ K}$ (d) $T = 343 \text{ K}$

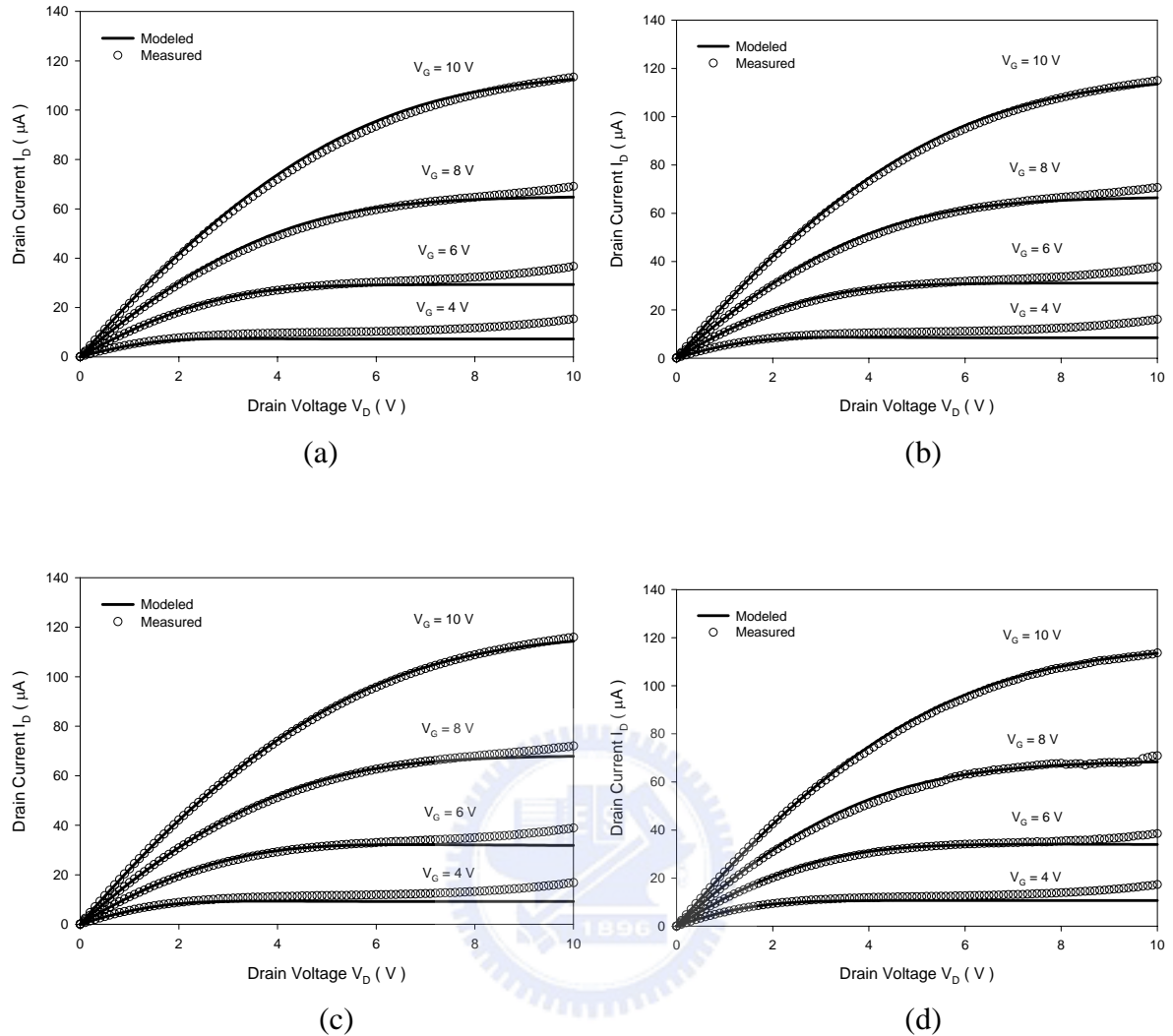


Fig. 3-32 The comparison of measured (symbols) and modeled (solid line) $I-V$ output characteristics for $W/L = 6 \mu\text{m} / 12 \mu\text{m}$ n-channel poly-Si TFTs annealed with laser power 100 W. (a) $T = 298 \text{ K}$ (b) $T = 313 \text{ K}$ (c) $T = 328 \text{ K}$ (d) $T = 343 \text{ K}$

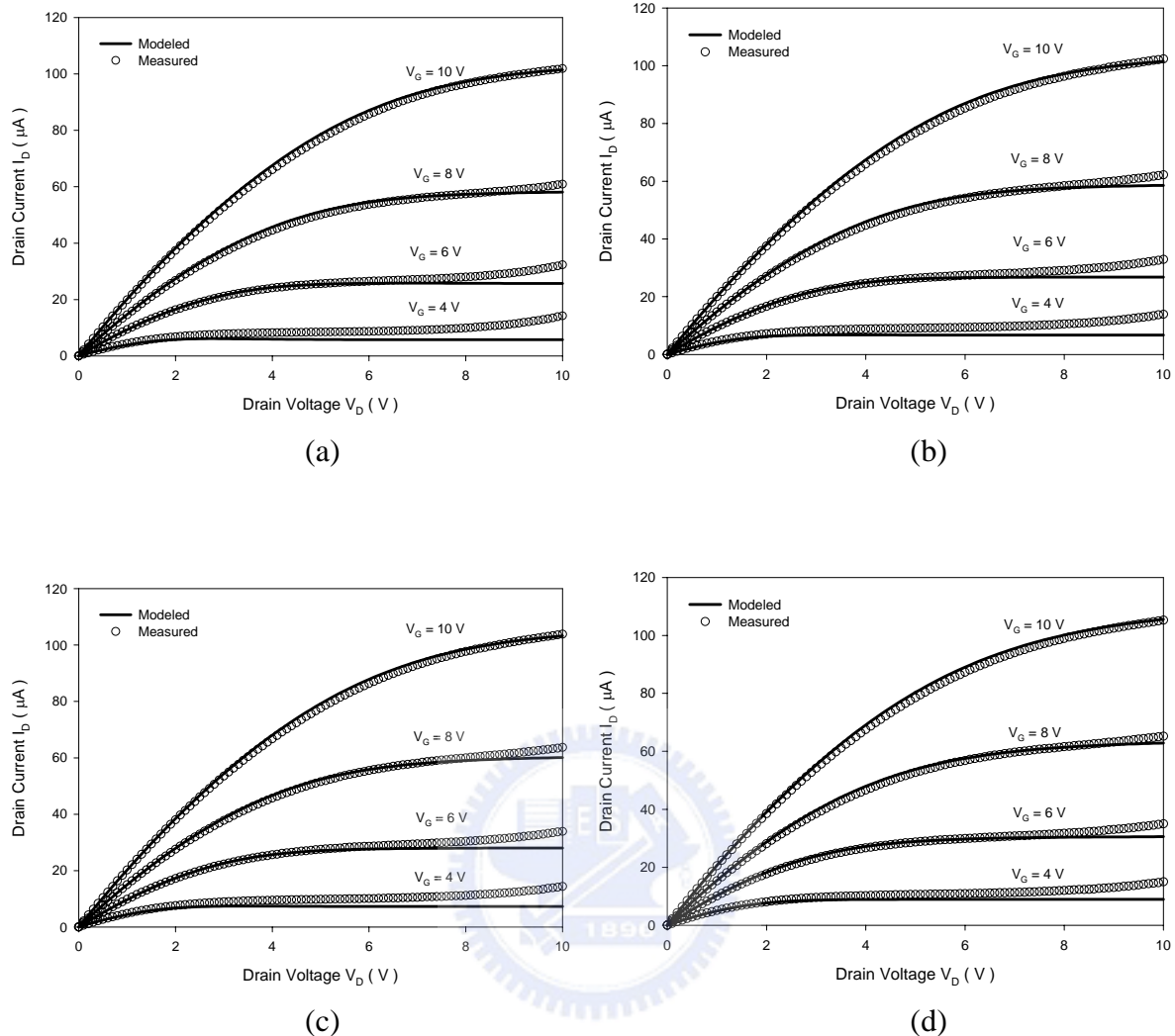


Fig. 3-33 The comparison of measured (symbols) and modeled (solid line) $I-V$ output characteristics for $W/L = 6 \mu m / 12 \mu m$ n-channel poly-Si TFTs annealed with laser power 95 W. (a) $T = 298 K$ (b) $T = 313 K$ (c) $T = 328 K$ (d) $T = 343 K$

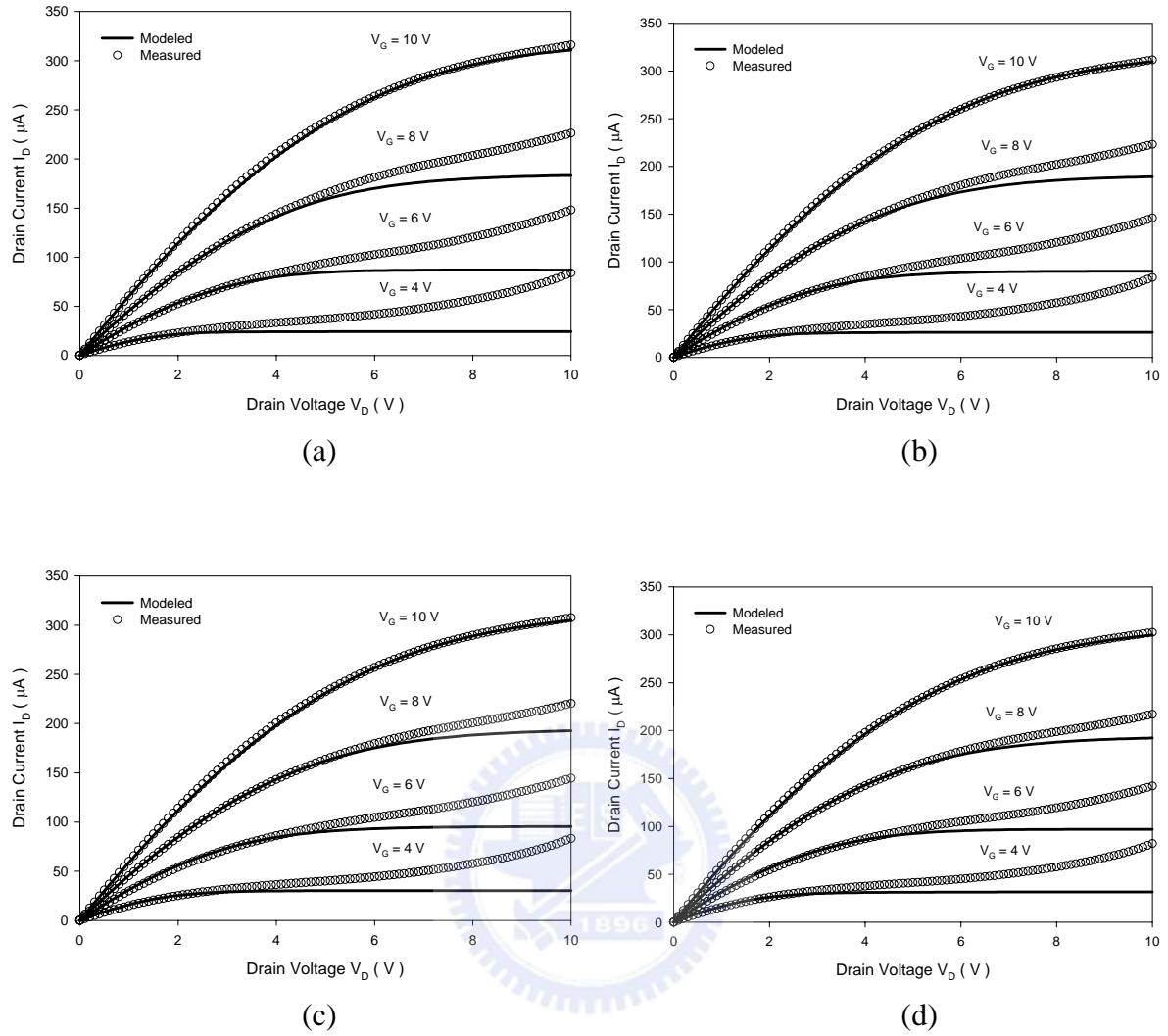


Fig. 3-34 The comparison of measured (symbols) and modeled (solid line) $I-V$ output characteristics for $W/L = 6 \mu\text{m} / 6 \mu\text{m}$ n-channel poly-Si TFTs annealed with laser power 110 W. (a) $T = 298 \text{ K}$ (b) $T = 313 \text{ K}$ (c) $T = 328 \text{ K}$ (d) $T = 343 \text{ K}$

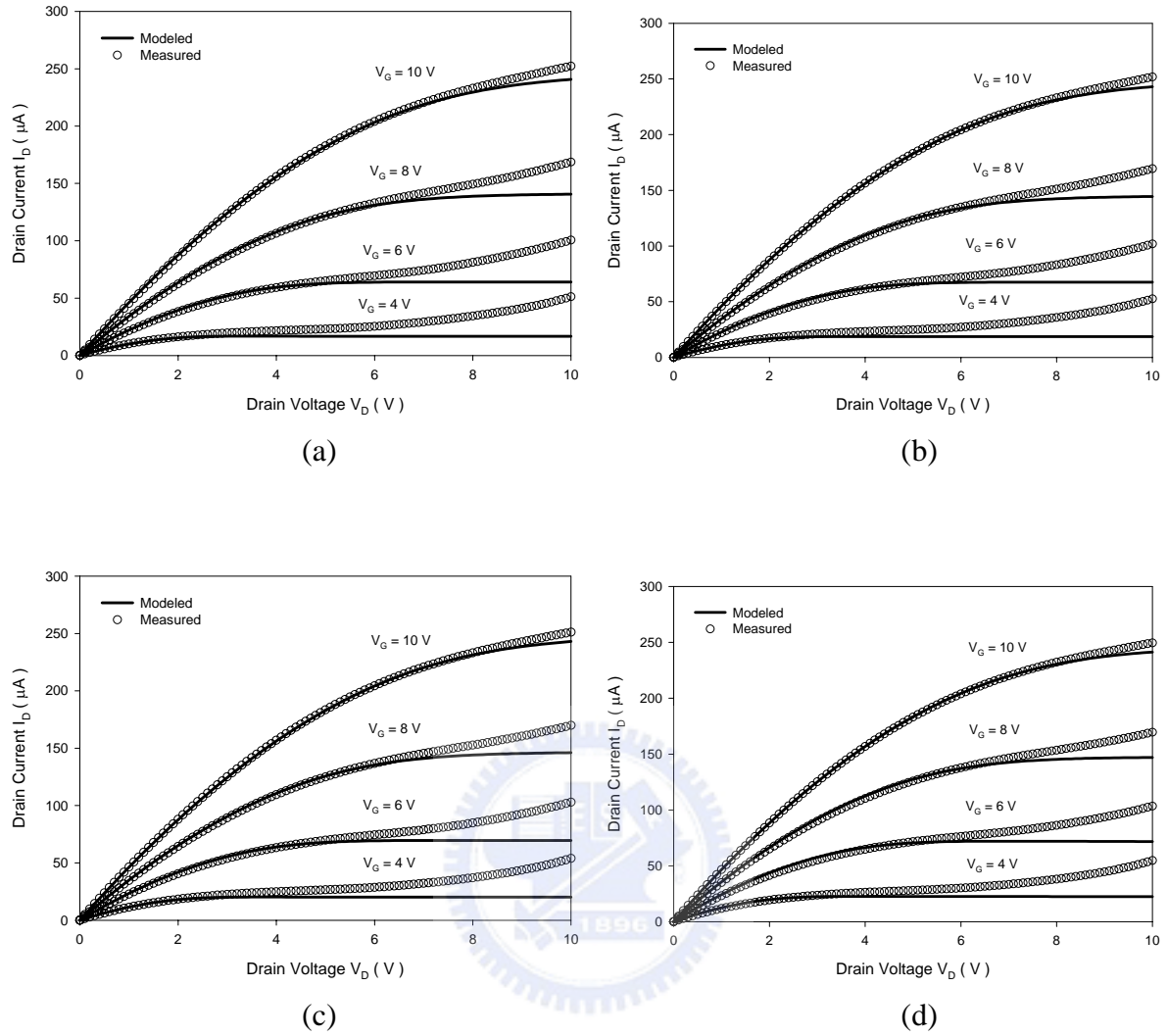


Fig. 3-35 The comparison of measured (symbols) and modeled (solid line) $I-V$ output characteristics for $W/L = 6 \mu\text{m} / 6 \mu\text{m}$ n-channel poly-Si TFTs annealed with laser power 100 W. (a) $T = 298 \text{ K}$ (b) $T = 313 \text{ K}$ (c) $T = 328 \text{ K}$ (d) $T = 343 \text{ K}$

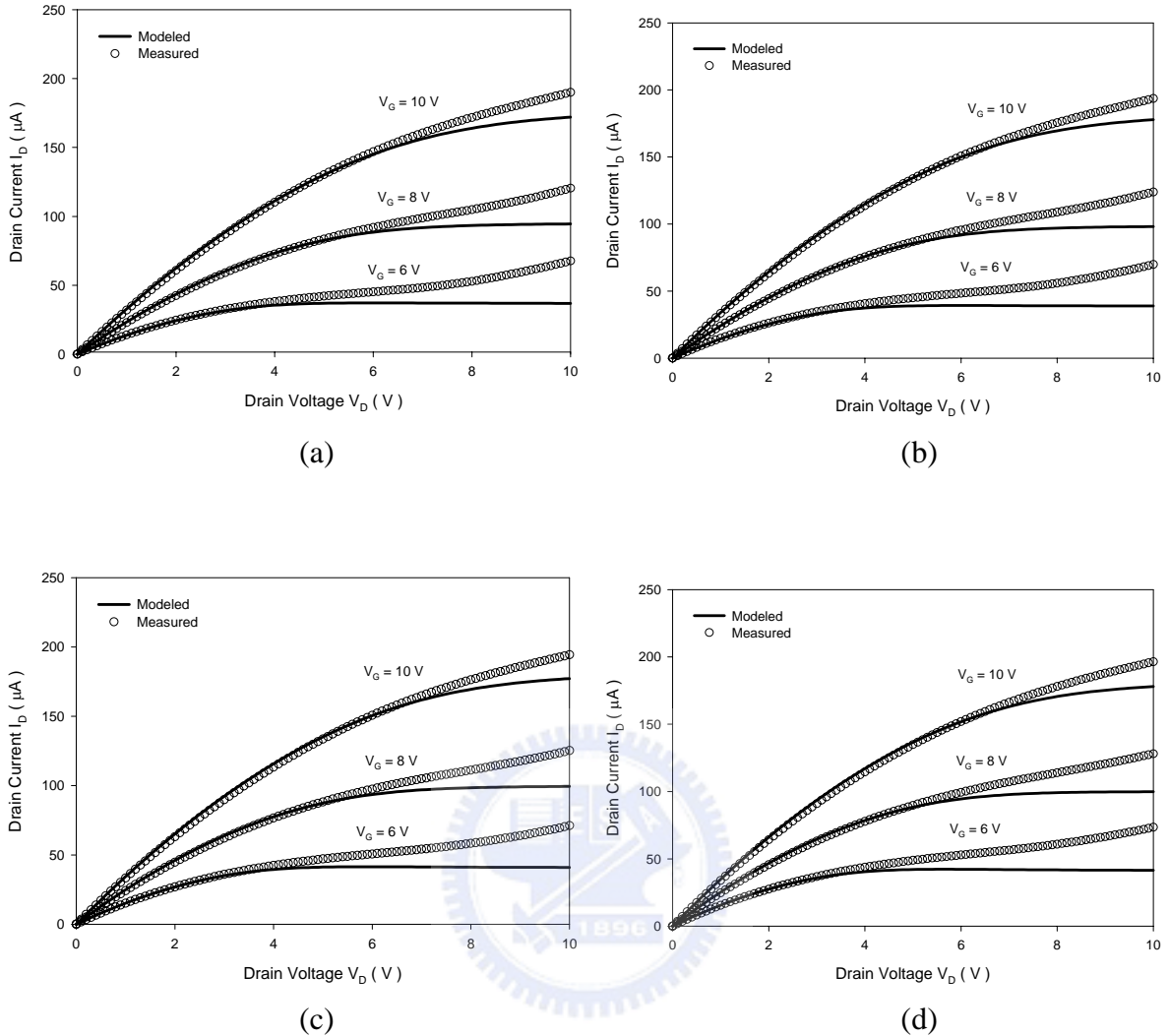


Fig. 3-36 The comparison of measured (symbols) and modeled (solid line) $I-V$ output characteristics for $W/L = 6 \mu\text{m} / 6 \mu\text{m}$ n-channel poly-Si TFTs annealed with laser power 95 W.
(a) $T = 298 \text{ K}$ (b) $T = 313 \text{ K}$ (c) $T = 328 \text{ K}$ (d) $T = 343 \text{ K}$